bioRxiv preprint doi: https://doi.org/10.1101/2020.02.11.944157; this version posted February 12, 2020. The copyright holder for this preprint (which was not certified by peer review) is the author/funder, who has granted bioRxiv a license to display the preprint in perpetuity. It is made available under aCC-BY-NC-ND 4.0 International license.

Small-molecule inhibition of Lats kinases promotes Yap-dependent proliferation in postmitotic mammalian tissues

Nathaniel Kastan[a,1], Ksenia Gnedeva[a,b,1,*], Theresa Alisch[a], Aleksandra A. Petelski[a,2], David J. Huggins[c], Jeanne Chiaravalli[d,3], Alla Aharanov[e], Avraham Shakked[e], Eldad Tzahor[e], Aaron Nagiel[f], Neil Segil[b], and A. J. Hudspeth[a,4,*]

Corresponding author: Dr. A. J. Hudspeth
Laboratory of Sensory Neuroscience
The Rockefeller University
New York, NY 10065
Telephone: 212 / 327-7351
E-mail: hudspaj@rockefeller.edu

Keywords: cardiomyocyte, hair cell, Hippo pathway, inner ear, Müller glia, supporting cell, Taz, utricle

[a] Howard Hughes Medical Institute and Laboratory of Sensory Neuroscience, The Rockefeller University, New York, NY 10065, USA

[b] Eli and Edythe Broad CIRM Center for Regenerative Medicine and Stem Cell Research and Tina and Rick Caruso Department Otolaryngology-Head and Neck Surgery, University of Southern California, Los Angles, CA 90033, USA

bioRxiv preprint doi: https://doi.org/10.1101/2020.02.11.944157; this version posted February 12, 2020. The copyright holder for this preprint (which was not certified by peer review) is the author/funder, who has granted bioRxiv a license to display the preprint in perpetuity. It is made available under aCC-BY-NC-ND 4.0 International license.

[c] Tri-Institutional Therapeutics Discovery Institute, New York, NY 10021, USA; Department of Physiology and Biophysics, Weill Cornell Medical College of Cornell University, New York, NY 10065, USA

[d] High-Throughput Screening Resource Center, The Rockefeller University, New York, NY 10065, USA

[e] Department of Molecular Cell Biology, Weizmann Institute of Science, Rehovot 7610001, Israel

[f] Vision Center, Department of Surgery, Children's Hospital Los Angeles, Los Angeles, CA, USA; Saban Research Institute, Children's Hospital Los Angeles, Los Angeles, CA, USA; USC Roski Eye Institute, Department of Ophthalmology, Keck School of Medicine, University of Southern California, Los Angeles, CA, USA

[1] These authors contributed equally to the research.

[2] Current address: Department of Bioengineering and Barnett Institute, Northeastern University, Boston, MA 02115, USA

[3] Current address: Institut Pasteur, 25-28 Rue du Dr. Roux, Paris 75015, France

[4] Lead Contact

*To whom correspondence should be directed at <gnedeva@usc.edu> or <hudspaj@rockefeller.edu>

bioRxiv preprint doi: https://doi.org/10.1101/2020.02.11.944157; this version posted February 12, 2020. The copyright holder for this preprint (which was not certified by peer review) is the author/funder, who has granted bioRxiv a license to display the preprint in perpetuity. It is made available under aCC-BY-NC-ND 4.0 International license.

Summary

Hippo signaling is an evolutionarily conserved pathway that restricts organ growth during development and suppresses regeneration in mature organs[1–3]. Using a high-throughput phenotypic screen, we have identified a potent, non-toxic, and reversible inhibitor of Hippo signaling. An ATP-competitive inhibitor of Lats kinases, the compound causes Yap-dependent proliferation of murine supporting cells in the inner ear, murine cardiomyocytes, and human Müller glia in retinal organoids. RNA sequencing indicates that the substance fosters both the G1-S and G2-M checkpoint transitions and yields supporting cells capable of transdifferentiation. Upon withdrawal of the compound, a subset of supporting cells move their nuclei into the hair-cell layer and express genes characteristic of hair cells. Viral transfection of Atoh1 induces the expression of hair cell-specific proteins in progeny. The compound promotes the initial stages of the proliferative regeneration of hair cells, a process thought to be permanently suppressed in the adult mammalian inner ear.

Introduction

Initiated in response to injury, regeneration is a complex process that can restore the structure and function of damaged tissue. Some adult mammalian tissues retain a gradually declining regenerative capability. Regeneration occurs either by activation and amplification of resident stem cells, as in the epithelia of the skin and intestine, or through cellular de-differentiation and proliferation, as in the liver. In other instances, such as central nervous and cardiac-muscle tissues, cells exhibit little or no potential for regeneration after injury[1,4,5].

One prominent example of a mammalian organ with poor regenerative capacity is the inner ear[6,7]. The auditory and vestibular sensory epithelia of all vertebrates possess only two major cell types: supporting cells, which play homeostatic and architectural roles,

bioRxiv preprint doi: https://doi.org/10.1101/2020.02.11.944157; this version posted February 12, 2020. The copyright holder for this preprint (which was not certified by peer review) is the author/funder, who has granted bioRxiv a license to display the preprint in perpetuity. It is made available under aCC-BY-NC-ND 4.0 International license.

and mechanosensitive hair cells. In non-mammalian vertebrates such as birds, lost hair cells are replaced by residual supporting cells that transdifferentiate into new sensory receptors either directly or after undergoing division[8]. Although modest numbers of hair cells regenerate through supporting-cell transdifferentiation in the neonatal mammalian cochlea[9] and in neonatal and adult vestibular organs[10], after the first postnatal week no proliferative response occurs following damage[11,12].

In view of its fundamental roles in development, proliferation, stem-cell maintenance, and de-differentiation, Hippo signaling is an inviting target for driving regeneration[1,3]. The canonical Hippo pathway is a highly conserved signal-transduction cascade that comprises two pairs of core kinases. When proliferation is unwarranted, Mst1 and Mst2 phosphorylate Lats1 and Lats2; these proteins in turn phosphorylate the transcriptional co-activator Yap and its homolog Taz, which as a result are sequestered and degraded in the cytoplasm. When the pathway is inactive, Yap enters the nucleus, interacts with transcription factors of the Tead family, and initiates cell division[2]. Yap signaling integrates a variety of information from the cellular environment, including biomechanical cues, cell density, cell polarity, metabolic challenges, and signals such as Notch and Wnt. The Hippo cascade is the conduit through which much, but not all, of this information is integrated into a decision regarding Yap activation[13].

The regenerative potential of the Hippo pathway has become abundantly clear in numerous organs, including the heart[5,14–16], retina[17], liver, and intestine[18]. We earlier demonstrated that Hippo signaling limits the size of the developing murine utricle, a vestibular sensory organ, and that the Yap-Tead complex is active during—and necessary for—proliferative regeneration in the neonatal utricle[19]. These observations suggested that chemical activation of Yap signaling might engender supporting-cell proliferation in adult tissue, a key missing step in the regeneration of the mammalian inner ear. We therefore conducted a small-molecule screen for Yap activators.

bioRxiv preprint doi: https://doi.org/10.1101/2020.02.11.944157; this version posted February 12, 2020. The copyright holder for this preprint (which was not certified by peer review) is the author/funder, who has granted bioRxiv a license to display the preprint in perpetuity. It is made available under aCC-BY-NC-ND 4.0 International license.

Results

Identification of activators of Yap signaling

In some monolayer epithelial cultures, increased cell density leads to Hippo activation and thus retention and degradation of Yap protein, a process reminiscent of growth restriction during normal development[20,21,22]. To seek inhibitors of this process, we designed a high-throughput phenotypic screen for compounds that promote nuclear Yap translocation in confluent human cell cultures (Fig. 1A). After testing three lines, we chose MCF 10A mammary epithelial cells, which demonstrated a robust negative correlation between cellular confluence and the fraction of cells with nuclear Yap (Figs. 1B,C and S1A).

For the small-molecule screen, we seeded MCF 10A cells to achieve dense cultures in 384-well plates. A single compound was deposited in each well at a concentration of 10 μM. Every plate also included a positive control, sub-confluent cells, and a negative control, densely cultured cells, both exposed to dimethyl sulfoxide (DMSO) at a concentration equivalent to that in which the compounds were applied. After 24 hr incubation, we determined the fraction of the cells with nuclear Yap and compared that value to the median negative-control value (Fig. 1D). We also scored the total number of surviving cells in each well and eliminated the compounds that decreased the number by more than one standard deviation in comparison to the dense control cultures. Nontoxic compounds that increased nuclear Yap by more than one standard deviation in comparison to the negative control were scored as hits (Fig. S1B,C). Owing to the robustness of contact inhibition in the dense cell cultures, only six of the compounds screened met these criteria.

Yap-dependent proliferation of supporting cells evoked by TRULI

Using utricles isolated from mice eight to twelve weeks of age , we next tested the effects of the the six compounds identified in the screen. Four elicited appreciable Yap nuclear

bioRxiv preprint doi: https://doi.org/10.1101/2020.02.11.944157; this version posted February 12, 2020. The copyright holder for this preprint (which was not certified by peer review) is the author/funder, who has granted bioRxiv a license to display the preprint in perpetuity. It is made available under aCC-BY-NC-ND 4.0 International license.

translocation, but only two evoked supporting-cell proliferation. Of the two proliferation-inducing compounds, one required a concentration in excess of 100 μM and appeared toxic to hair cells. The final compound, *N*-(3-benzylthiazol-2(3H)-ylidene)-1H-pyrrolo[2,3-b]pyridine-3-carboxamide, drove robust Yap nuclear translocation after 24 hr of treatment at a concentration of 10 μM and caused a striking reduction in the level of Yap phosphorylation (Figs. 2A,B,D and S2A). After 5 d of treatment, this substance evoked robust re-entry into the cell cycle of adult utricular supporting cells (Fig. 2C,E). For the sake of brevity we term this substance "TRULI."

We also tested the recently published inhibitor of Mst1 and Mst2 kinases[18], XMU-MP-1. Although XMU-MP-1 reduced the amount of phospho-Yap, it decreased the total Yap by a greater amount so that the ratio actually increased (Fig. S2A,B). No significant proliferation was observed after 5 d of treatment (Fig. S2C).

We additionally assessed the effect of TRULI in the murine cochlea. Although a proliferative response was observed in Kölliker's organ, where progenitor-like cells capable of differentiating into both hair and supporting cells reside[23,24], all but the most lateral rows of supporting cells in the organ of Corti remained postmitotic after treatment with TRULI (Fig. S3).

To test whether the proliferative effect of TRULI is exerted through Yap, we co-treated explants with TRULI and 5 μM verteporfin, an inhibitor of the interaction between Yap or Taz and Tead transcription factors[25]. Consistent with the hypothesis, co-treatment with verteporfin precluded a proliferative response (Fig. 2C,E). To confirm these results, we used *SOX2-Cre*^{ER} and *Yap*$^{fl/fl}$ mice to generate inducible conditional-knockout animals deficient for the protein in the sensory organs of the inner ear[26,27]. Owing to the stability of Yap protein[28], Cre-mediated recombination was induced either 7 d or 14 d prior to utricular explantation and culture. In the utricles isolated from *Yap*$^{fl/fl}$ littermate mice lacking Cre recombinase, treatment with TRULI elicited robust proliferation of supporting

bioRxiv preprint doi: https://doi.org/10.1101/2020.02.11.944157; this version posted February 12, 2020. The copyright holder for this preprint (which was not certified by peer review) is the author/funder, who has granted bioRxiv a license to display the preprint in perpetuity. It is made available under aCC-BY-NC-ND 4.0 International license.

cells (Fig. 2F,G). In contrast, in utricles explanted from Yap knockout animals, proliferation was significantly reduced.

Blockage of Lats-dependent Yap phosphorylation by TRULI

We investigated the mechanism of TRULI's inhibition in the MCF 10A cell line. After treatment of confluent cells with 10 μM of TRULI for 24 hr, protein blotting revealed that the Hippo signaling cascade was intact through the phosphorylation of the activation loops of Lats1 (S909) and Lats2 (S872) (Fig. 3A). However, the phosphorylation of Yap at residue S127 was decreased, suggesting that TRULI is—directly or indirectly—an inhibitor of Lats kinases.

To confirm this inference we turned to HEK293A cells, which activate Lats kinases in response to serum starvation and thus inactivate Yap to prevent growth during nutrient deprivation[29,30]. We pre-treated 80 % confluent HEK293A cells with 10 μM TRULI for 1 hr, followed by 30 min of serum starvation. In control cultures, starvation elicited robust phosphorylation of Lats1 at S909 and the consequent phosphorylation of Yap at S127 (Fig. 3B). In cultures pre-treated with TRULI, however, serum starvation failed to evoke phosphorylation of Yap despite the activation of Lats1. Even under treated, serum-fed conditions, phospho-Yap levels were below those of serum-fed control cells. Negative-feedback regulation in response to elevated Yap activity might explain why the amount of Lats1 S909 was enhanced in the treated, serum-fed condition[31]. These results together confirmed that TRULI interferes with the ability of Lats kinases to phosphorylate Yap.

Direct inhibition of Lats1 and Lats2 by TRULI

The structure of TRULI includes a 7-azaindole moiety characteristic of the hinge-binding motifs of ATP-competitive kinase inhibitors (Fig. 3C) Because there are no known crystal structures of the Lats kinases, we created a homology model from the crystal structure of the ATP pocket of similar kinase ROCK1 bound to a small-molecule inhibitor containing a 7-azaindole moiety. A putative structure of the complex between Lats1 and TRULI was

bioRxiv preprint doi: https://doi.org/10.1101/2020.02.11.944157; this version posted February 12, 2020. The copyright holder for this preprint (which was not certified by peer review) is the author/funder, who has granted bioRxiv a license to display the preprint in perpetuity. It is made available under aCC-BY-NC-ND 4.0 International license.

then generated by molecular docking (Fig. 3D). Because the predicted protein-ligand contact residues of Lats1 and Lats2 are almost completely conserved, the model suggests that TRULI can bind either with similar inhibitory potencies.

To test our speculations about the mechanism of TRULI inhibition, we optimized an *in vitro* kinase assay using truncated forms of Lats1 (residues 589-1130) and Lats2 (residues 553-1088) that include primarily the kinase domains (Fig. S4A-C). As a substrate we employed the peptide STK1, which is known to be phosphorylated by these enzymes[32]. Because we hypothesized TRULI was ATP-competitive, we first determined the Michaelis-Menten constants of Lats1 and Lats2 for ATP to be near 10 μM for both enzymes, at which we ran the initial *in vitro* kinase assays (Fig. S4A). Under these conditions, we found that TRULI directly inhibits both Lats1 and Lats2 with a half-maximal inhibitory concentration (IC_{50}) of 0.2 nM (Figs. 3E and S4D), whence the name TRULI: “The Rockefeller University Lats inhibitor." In support of our hypothesis, increases in ATP concentrations yielded positive shifts in the IC_{50} (Fig. 3E).

To determine the potency of TRULI in living cells, we evaluated the content of total Yap and phospho-Yap in HEK293A cells serum-starved in the presence of various concentrations of TRULI. The half-maximal effective concentration of the compound was EC_{50} = 510 nM (Fig. 3F).

To assess the selectivity of TRULI, we first compared the sequences of the putative ATP-binding residues of Lats1 and Lats2 with those of other members of the AGC kinase family (Tables S1 and S2)[33]. To determine which of these potential off-target kinases are bound, we tested TRULI in a broad kinome-binding panel[34]. Of the 314 kinases tested, 34 bound TRULI more strongly than Lats1 (Table S3). These values represent an upper bound: although only kinases bound by a small molecule might be relevant, not all such enzymes are functionally inhibited. The selectivity score, or percentage of kinases for which the inhibitor has a half-maximal concentration of binding displacement below 1 μM, was 18.1. This value compares with control values of 86.0 for

bioRxiv preprint doi: https://doi.org/10.1101/2020.02.11.944157; this version posted February 12, 2020. The copyright holder for this preprint (which was not certified by peer review) is the author/funder, who has granted bioRxiv a license to display the preprint in perpetuity. It is made available under aCC-BY-NC-ND 4.0 International license.

the broad-spectrum kinase inhibitor staurosporine and of 18.8 for dasatinib, a clinically approved selective inhibitor of tyrosine kinases. To assess whether some of the kinases identified in both approaches were in fact functionally inhibited, we measured IC_{50} values against four kinases that were high on both lists and represented by multiple family members[35]. Some were affected significantly more strongly than others (Table S4). Although it will be necessary to explore other potential off-target kinases, particularly in a tissue-specific context, these data demonstrate that TRULI is a potent, direct, and relatively selective inhibitor of Lats1 and Lats2.

Gene-expression consequences of TRULI treatment

To characterize the consequences of Lats-kinase inhibition with TRULI, we analyzed the changes in gene expression triggered by the compound after 5 d of treatment. To facilitate the sorting of supporting cells from treated utricles, we utilized *Lfng-EGFP* mice, whose supporting cells bear a fluorescent tag[36]. Principal-component analysis of RNA-sequencing data revealed that almost 60 % of the variance between TRULI-treated and control samples could be explained by the first principal component and that the three samples collected under each condition clustered closely along that axis (Fig. 4A). Over 70 % of differentially expressed genes whose expression changed by at least a factor of two were upregulated after treatment (Fig. 4B). Gene ontology analysis[37] demonstrated that the terms associated with regulation of the cell cycle were the most enriched amongst up-regulated genes (Fig. 4C).

To assess the biological relevance of the changes in gene expression triggered by TRULI, we compared the FPKM values for the differentially expressed genes to those from late embryonic (E17.5) utricular supporting cells. At that stage such cells remain highly plastic and are capable of both proliferation and differentiation into the new sensory receptors[38,39]. The expression levels for most cell cycle-related genes (gene-ontology term 0007049) that were differentially expressed in postnatal supporting cells after TRULI

bioRxiv preprint doi: https://doi.org/10.1101/2020.02.11.944157; this version posted February 12, 2020. The copyright holder for this preprint (which was not certified by peer review) is the author/funder, who has granted bioRxiv a license to display the preprint in perpetuity. It is made available under aCC-BY-NC-ND 4.0 International license.

treatment were highly similar to those in E17.5 supporting cells (Fig. 4D). In particular, the genes specific to the G1-S and G2-M stages of the cell cycle were significantly up-regulated by TRULI to the embryonic levels of expression (Fig. 4E,F). Consistent with the pro-survival role of Yap-Tead signaling, TRULI repressed expression of a subset of inflammatory and pro-apoptotic genes.

The direct targets of the Yap-Tead complex have been identified in other contexts, such as in mammary cancer cells[40]. In accord with the compound's acting as an activator of nuclear Yap signaling, over 90 % of confirmed direct downstream targets of Yap-Tead complex identified within differentially expressed genes were up-regulated in response to TRULI treatment (Fig. 4G,H). Consistent with our demonstration of a role for Yap in the development of the utricular sensory epithelium[41], most of these Yap-target genes were also highly expressed in E17.5 supporting cells.

Inhibition of Lats kinases by TRULI had no apparent toxic effect on utricular supporting cells: genes associated with cell death (gene-ontology term 0008219) remained unchanged after treatment (Fig. 4I).

Supporting-cell differentiation after TRULI treatment

To determine whether the increased supporting-cell proliferation triggered by TRULI can be reversed, we performed EdU pulse-chase experiments following TRULI treatment. The mitogenic effects of Lats inhibition persisted for 24-48 hr after drug withdrawal, for many supporting cells incorporated EdU during that interval (Fig. S5). However, most supporting cells exited the cell cycle thereafter.

Forcing postmitotic cells to re-enter the cell cycle can result in arrest at the G1-S or G2-M checkpoint transition and consequently in programmed cell death[42]. To evaluate the long-term outcome of Lats inhibition on supporting cells, we treated three-week-old *Lfng-GFP* utricles with TRULI for 5 d followed by 5 d of withdrawal. RNA-sequencing analysis demonstrated that the levels of expression for the cell cycle-related genes and

bioRxiv preprint doi: https://doi.org/10.1101/2020.02.11.944157; this version posted February 12, 2020. The copyright holder for this preprint (which was not certified by peer review) is the author/funder, who has granted bioRxiv a license to display the preprint in perpetuity. It is made available under aCC-BY-NC-ND 4.0 International license.

the direct Yap targets that were highly up-regulated upon TRULI treatment were indistinguishable between TRULI-treated and control supporting cells (Fig. S6). In addition, we did not observe enrichment for pro-apoptotic genes after TRULI treatment. Instead, the up-regulated genes were associated with the gene-ontology terms related to hair-cell development and function (Fig. 5A,B). These included the genes for hair cell-specific transcription factors such as Atoh1, Pou4f3, Gfi1, and Lhx3 as well as genes encoding important hair-cell proteins: nonmuscle myosins (Myo15, Myo7A, Myo5A), Ca^{2+} sensors and buffers (Otof, Calb, S100), and transduction machinery (Tmc1, Tomt).

Because the foregoing results suggested the transdifferentiation of newly formed supporting cells, we sought newly formed hair cells by EdU incorporation. Treatment with TRULI did not affect hair-cell or supporting-cell survival, confirming that the compound is not toxic at the effective concentration (Fig. 5C,D). Although almost none of the cells expressed Pou4f3 or Myo7A, many of the EdU-positive supporting-cell nuclei migrated into the hair-cell layer. This pattern is consistent with the first stages of transdifferentiation.

To test whether supporting cells were capable of giving rise to hair cells after they had proliferated, we treated P21 utricles with TRULI and virally transfected the cultures with *Atoh1-RFP* upon drug withdrawal. Demonstrating a capacity for transdifferentiation into putative hair-cell precursors, many EdU- and Pou4f3-positive cells were observed after *Atoh1* transfection (Fig. S6D).

Effects of TRULI on cardiomyocytes and Müller glia

Because the regenerative effects of activating Yap in organs such as the retina and heart have been characterized extensively[5,14,15,17], we investigated whether TRULI treatment is effective in eliciting cellular proliferation in these contexts.

The proliferative capacity of cardiomyocytes in culture and the capacity of the heart to regenerate decline sharply after birth[5]. To ascertain whether TRULI activates Yap and induces regeneration, we exposed P0 murine cardiomyocytes to TRULI for 3 d. In control

bioRxiv preprint doi: https://doi.org/10.1101/2020.02.11.944157; this version posted February 12, 2020. The copyright holder for this preprint (which was not certified by peer review) is the author/funder, who has granted bioRxiv a license to display the preprint in perpetuity. It is made available under aCC-BY-NC-ND 4.0 International license.

cultures, protein blotting revealed high levels of phospho-Yap indicative of Hippo activity. TRULI treatment reduced the proportion of phosphorylated Yap and induced cardiomyocyte proliferation, as demonstrated by a significant increase in the percentage of cells positive for the markers Ki67 and phosphorylated histone H3 (Fig. 6A-E). Moreover, treated cells developed cytoskeletal rearrangements and protrusions and decreased in size, phenotypes consistent with de-differentiation and proliferation, respectively (Fig. 6F,G)[43].

Yap activation may permit retinal regeneration in mammals by stimulating the proliferation of Müller glial cells, progenitors with a capacity to differentiate into photoreceptors and neurons[17,44]. To test whether TRULI induces the proliferation of Müller glia, we used retinal organoids derived from human induced pluripotent stem cells. As expected, Müller cells remained largely quiescent in control cultures. In organoids treated for 5 d with 10 μM TRULI, however, Müller cells exhibited a robust increase in proliferation (Fig. 6H-K).

Discussion

Most experiments demonstrating the regenerative effects of Yap activation in mammalian tissues have used transgenesis, viral transfection, or indirect approaches such as activation of G protein-coupled receptors by sphingosine-1-phosphate or epinephrine. Although these studies have provided proof-of-principle results, manipulation of Yap signaling with small molecules represents a more feasible translational approach. In fact, the only other published inhibitor of the Hippo pathway, XMU-MP-1, activates Yap signaling and facilitates healing of the liver and intestinal epithelium after damage[18]. It is noteworthy, however, that in our hands XMU-MP-1 did not promote supporting-cell proliferation in the utricle. This result suggests that other enzymes function redundantly to Mst kinases in the sensory epithelia. These likely include the Map4K kinases, which activate Lats kinases in other contexts[45]. In fact, our RNA-sequencing data revealed that

bioRxiv preprint doi: https://doi.org/10.1101/2020.02.11.944157; this version posted February 12, 2020. The copyright holder for this preprint (which was not certified by peer review) is the author/funder, who has granted bioRxiv a license to display the preprint in perpetuity. It is made available under aCC-BY-NC-ND 4.0 International license.

Map4K2, Map4K3, and Map4K4 are all highly expressed in the adult murine utricle. To our knowledge, no enzymes are broadly redundant to Lats1 and Lats2. Inhibition of Lats kinases with TRULI might therefore provide an effective means of inactivating Hippo signaling in a variety of tissues.

Re-entry into the cell cycle is only one component of regeneration; the daughter cells must also assume their correct cell fates. Our data suggest that, in addition to inducing proliferation, TRULI treatment leaves newly formed supporting cells in a plastic state. After undergoing division, supporting cells re-enter G0 upon drug withdrawal, and many cells shift their nuclei into the hair-cell layer and activate expression of characteristic hair-cell genes; the pattern is strikingly similar to the regenerative response in non-mammalian vertebrates[8]. Because these cells can initiate transdifferentiation upon Atoh1 overexpression, combining Hippo inhibition with inhibition of Notch signaling or Atoh1 gene therapy might constitute an effective approach to restoring hair cells.

In contrast to the robust response in the adult murine utricle, the vast majority of supporting cells in the neonatal cocTiktaalikhlea remained quiescent after 5 d of TRULI treatment. A wave of transcriptional up-regulation of *Cdkn1B*, the gene encoding P27Kip1, is known to control both the timing and the pattern of cell-cycle exit in the organ of Corti[46]. This process seems absent from the utricle. Activation of Wnt signaling promotes proliferation in the neonatal organ of Corti, but the effect primarily involves Kölliker's organ and the lateral Hensen's cells[47,48,49,50]. This pattern resembles that observed after treatment with TRULI. To facilitate cell-cycle re-entry, the organ of Corti might require a more prolonged exposure to proliferative stimuli or treatments that target multiple signaling pathways.

Although pharmacological manipulation of the Hippo pathway might prove useful in dealing with many human diseases, much remains unknown about the potential pitfalls of Lats inhibition. In the context of the Hippo pathway Lats1 and Lats2 are considered redundant, but each paralog also has unique functions such as estrogen-mediated

bioRxiv preprint doi: https://doi.org/10.1101/2020.02.11.944157; this version posted February 12, 2020. The copyright holder for this preprint (which was not certified by peer review) is the author/funder, who has granted bioRxiv a license to display the preprint in perpetuity. It is made available under aCC-BY-NC-ND 4.0 International license.

signaling and p53 regulation, respectively. Furthermore, Lats kinases and Yap have ancient and conserved non-Hippo functions in spindle-assembly checkpoints and cytokinesis[51]. TRULI also offers the ability to investigate these non-Hippo functions of Lats kinases, and it would be prudent to understand the implications of Lats inhibition on these pathways prior to therapeutic endeavors.

Another potential concern about Lats inhibition is oncogenic transformation. In this regard the effect of systemic inhibition of Mst kinases is encouraging[18]: even after long-term administration, no oncogenic transformation was observed in mice treated with XMU-MP-1. Moreover, the impact of Lats inhibition might be mitigated by local application in isolated fluid compartments such as the endolymph of the inner ear, vitreous humor of the retina, and pericardium of the heart. Finally, the relationship of Yap to cancer is complex. Yap activation is a marker for poor prognosis in some cancers, but the opposite is true in other instances[52]. Mutations of proteins in the Hippo pathway are rarely causative of cancer, but are instead secondary to the molecular changes associated with tumorigenesis[3]. In fact, activation of Yap through deletion of Lats kinases in certain syngenic tumors *decreases* their progression and metastasis in immune-competent mice by augmenting the immune response[53].

In summary, TRULI is a potent, non-toxic, and reversible inhibitor of Lats kinases, and thus a powerful tool for exploring the role of Hippo signaling in a variety of biological contexts. As expected on the basis of prior work, Yap activation with TRULI induces the proliferation of murine neonatal cardiomyocytes in primary culture and of human Müller glia in retinal organoids. Moreover, the sensory epithelia of the inner ear now join the list of tissues amenable to Yap-mediated regeneration. In view of the ubiquity of these effects, it is plausible that drugs related to this novel thiazolimine class will prove useful in therapeutic contexts.

bioRxiv preprint doi: https://doi.org/10.1101/2020.02.11.944157; this version posted February 12, 2020. The copyright holder for this preprint (which was not certified by peer review) is the author/funder, who has granted bioRxiv a license to display the preprint in perpetuity. It is made available under aCC-BY-NC-ND 4.0 International license.

Materials and Methods

Animal care and strains

Experiments were conducted in accordance with the policies of the Institutional Animal Care and Use Committees of The Rockefeller University, the University of Southen Califiornia, and the Weizmann Institute of Science.

Swiss Webster mice were obtained from Charles River Laboratories. *Sox2-Cre*^{ER}, α*MHC-Cre*, and *ROSA26-tdTomato* mice were obtained from the Jackson laboratory. *Yap*$^{fl/fl}$ (Zhang et al., 2010) were provided by Dr. Martin, Baylor College of Medicine.

Cardiac muscle cells were lineage-traced with tdTomato-fluorescent protein by intercrossing αMHC-cre mice[54], which exhibit highly efficiency recombination in cardiomyocytes, with ROSA26-tdTomato mice[55] that require Cre-mediated recombination for expression. Both lines were maintained on a C57BL/6 background.

Chemical libraries

A total of 140,238 different compounds from a library at The Rockefeller University High-Throughput and Spectroscopy Resource Center were chosen by a quantitative estimate of drug-likeness score[56]. The compounds originated in the following commercially available libraries: ChemDiv (San Diego, CA), Enamine (Monmouth Junction, NJ), BioFocus (Charles River, Wilmington, MA), ChemBridge (San Diego, CA), Specs (Zoetermeer, The Netherlands), Life Chemicals (Niagara, Canada), and AMRI (Albany, NY). Compound stocks were stored in 384-well polypropylene plates at a final concentration of 5 mM in DMSO at -30 ˚C.

High-throughput screen for small-molecule activators of nuclear Yap

Three human epithelial cell lines, one human embryonic kidney 293 line (HEK293T), and two human mammary gland epithelia lines (MDA-MB and MCF 10A), were tested for the screen. Of the three lines, only MCF 10A cells display a reproducible correlation between

bioRxiv preprint doi: https://doi.org/10.1101/2020.02.11.944157; this version posted February 12, 2020. The copyright holder for this preprint (which was not certified by peer review) is the author/funder, who has granted bioRxiv a license to display the preprint in perpetuity. It is made available under aCC-BY-NC-ND 4.0 International license.

the number of cells seeded and the number of cells adhered after 24h in culture and thus were selected for the screen.

MCF 10A cells (ATCC CRL-10317) were cultured in a medium comprising DMEM/F12, 5 % horse serum (Invitrogen 16050-122), 20 ng/L epidermal growth factor (Millipore GF155), 0.5 mg/L hydrocortisone (Sigma H-0888), 100 ng/L cholera toxin (Sigma C-8052), 10 mg/L insulin (Sigma I-1882), and antibiotic-antimycotic solution. Cell cultures reached 100 % confluence at an approximate density of $3 \cdot 10^5$ cells per square millimeter.

For the small-molecule screen, chemical-library plates were thawed at room temperature and 0.1 µL of each compound was placed in a well of a 384-well assay plates (Greiner Bio-One) containing 10 µL of MCF 10A culture medium (PerkinElmer Janus with Nanohead). MCF 10A cells were then plated in 40 µL of MCF 10A culture medium to achieve a final concentration of 10 µM for each compound and 0.25 % (vol/vol; 35 mM) dimethyl sulfoxide. Negative (100 % confluent) and positive (25 % confluent) control wells included an identical concentration of the DMSO vehicle.

After 24 hr incubation, the cells were fixed, washed thrice in PBS, and immunolabeled for Yap. The nuclei were stained with 3 mM 4,6-diamidino-2-phenylindole dihydrochloride (DAPI). The plates were imaged automatically with a 10X objective lens on the ImageXpress XLS wide-field Micro reader (Molecular Devices, Sunnyvale, CA) with MetaXpress software (Molecular Devices). Using an empty plate to avoid out-of-focus images, we configured a laser-based autofocus routine for automatic well-bottom detection. We imaged DAPI and Yap conjugated to Alexa Fluor 488 with filter cubes for respectively DAPI (excitation, 350-400 nm; emission 415-480 nm) and FITC (excitation, 460-505 nm; emission, 510-565 nm). The acquisition system was configured to image one site per well. After the fluorescence of DAPI had been used to set the image-based autofocus, the exposure time for each fluorophore was determined with a negative-control well in which the fluorescence signal was set to 75 % of the camera's maximal intensity.

bioRxiv preprint doi: https://doi.org/10.1101/2020.02.11.944157; this version posted February 12, 2020. The copyright holder for this preprint (which was not certified by peer review) is the author/funder, who has granted bioRxiv a license to display the preprint in perpetuity. It is made available under aCC-BY-NC-ND 4.0 International license.

An image-segmentation application from MetaXpress software was used to automatically analyze the images. The number of cells was estimated by selecting an average size and intensity level above the local background in the DAPI channel.

A built-in translocation module that measured the intensity movement from one compartment to another was configured to determine the nuclear or cytoplasmic status of the Yap. These measurements were acquired first for the positive and negative control wells to determine an arbitrary threshold for the intensity ratio that characterized nuclear translocation *versus* cytoplasmic retardation of Yap. The same threshold was then applied to each well treated with a small-molecule to identify the substances that increased the number of cells with nuclear Yap without affecting cell survival. Positive controls were not used to normalize data, but to confirm whether the cells were healthy and behaving as expected.

Images were stored in the MDCStore database and analyzed using MetaXpress software (Molecular Devices). Output data were uploaded and analyzed using the CDD Vault from Collaborative Drug Discovery (Burlingame, CA).

The compounds showing over 10 % Yap nuclear translocation and over 5,000 cells per field were selected and the corresponding images were checked to verify the phenotype. To determine half-maximal inhibitory concentrations, the selected compounds were re-tested in concentration-response experiments by serially diluting by half for a total of ten dilutions to achieve assay concentrations ranging from 20 μM to 0.03 μM. IC_{50s} values were calculated by CDD software. Six compounds were confirmed in this secondary screen.

Small-molecule Lats inhibitor

The compound *N*-(3-benzylthiazol-2(3H)-ylidene)-1H-pyrrolo[2,3-b]pyridine-3-carboxamide (CAS number 1424635-83-5), of relative molecular mass 334.4 Da and

bioRxiv preprint doi: https://doi.org/10.1101/2020.02.11.944157; this version posted February 12, 2020. The copyright holder for this preprint (which was not certified by peer review) is the author/funder, who has granted bioRxiv a license to display the preprint in perpetuity. It is made available under aCC-BY-NC-ND 4.0 International license.

herein termed TRULI, was obtained from Enamine LLC (Z730688380, Monmouth Junction, NJ).

Dissection and culture of inner-ear sensory epithelia

Internal ears were dissected from mice euthanized with fluothane and placed into ice-cold Hank's balanced salt solution (HBSS; Gibco14025-092)[57].

Unless indicated otherwise, explanted cultures of the utricle and cochlea were maintained in an incubator at 37 ˚C in the presence of 5 % CO_2 and 95 % O_2. The complete growth medium comprised Dulbecco's modified Eagle medium with nutrient mixture F-12 (DMEM/F12) supplemented with 33 mM **D**-glucose (Sigma G8644), 19 mM $NaHCO_3$ (Sigma S8761), 15 mM HEPES (Sigma H0887), 1 mM glutamine (Sigma G8540), 5 mM nicotinamide (Sigma N0636), 40 μg/L epidermal growth factor (Sigma E9644), 20 μg/L fibroblast growth factor (Sigma F5392), insulin-transferrin-selenite solution (Sigma 11074547001), and antibiotic-antimycotic solution (Gibco 15240062).

For proliferation assays, utricles were cultured with 10 μM 5-ethynyl-2′-deoxyuridine (EdU) that was detected with click chemistry (Click-iT EdU imaging kit, Thermo C10340).

Culture of epithelial cells

MCF 10A cells were cultured as described above. HEK293A cells were maintained in DMEM (Gibco 11965-092), 10 % fetal bovine serum (Sigma F2442), and antibiotic-antimycotic solution. All cells were incubated at 37 ˚C in the presence of 5 % CO_2 and 95 % O_2.

Culture of primary cardiomyocytes

Cardiac muscle cells were lineage-traced with tdTomato-fluorescent protein by intercrossing α*MHC Cre* mice[54], which exhibit highly efficiency recombination in cardiomyocytes, with *ROSA26-tdTomato* mice[55] that require Cre-mediated recombination for expression. Both lines were maintained on a C57BL/6 background.

bioRxiv preprint doi: https://doi.org/10.1101/2020.02.11.944157; this version posted February 12, 2020. The copyright holder for this preprint (which was not certified by peer review) is the author/funder, who has granted bioRxiv a license to display the preprint in perpetuity. It is made available under aCC-BY-NC-ND 4.0 International license.

Neonatal primary cardiac cultures were isolated from P0 pups with a neonatal dissociation kit (Miltenyi Biotec,130-098-373) and homogenizer (gentleMACS). Cardiac cultures were seeded in gelatin-coated wells coated with 0.1 % gelatin (G1393, Sigma) in DMEM/F12 medium supplemented with 1% L-glutamine, 1 % sodium pyruvate, 1 % nonessential amino acids, 1 % penicillin-streptomycin solution, 5 % horse serum, and 10 % fetal bovine serum. After culture in 5 % CO_2 for 24 hr at 37 ˚C, the medium was replaced for an additional 72 hr with bovine serum-free medium containing 0.1 % (vol/vol) DMSO and, for experimental samples, 20 μM TRULI.

Culture of human pluripotent stem cells and retinal organoids

The WTC-11 line of induced pluripotent stem cells (Coriell Institute for Medical Research, Camden, NJ) was maintained using standard methods. Human retinal organoids were produced from these cells[58]. In three independent proliferation assays, five organoids 225-280 d of age per experimental condition were sampled in culture after incubation for 5 d in 10 μM TRULI and 10 μM EdU. The organoids used in the immunoblot analysis were 160-178 d of age and were incubated for 24 hr in 10 μM TRULI.

Immunohistochemistry of murine inner-ear sensory epithelia

Utricles were fixed in 4 % formaldehyde (Thermo 28906) for 1 hr at room temperature and then blocked for 2 hr at room temperature with 3 % bovine serum albumin (BSA; Jackson AB 2336846), 3 % normal donkey serum (Sigma-Aldrich D9663), and 0.3 % Triton X-100 (Sigma 93443), in Tris-buffered saline solution (Thermo 28358).

The primary antisera—goat anti-Sox2 (R&D AF2018), rabbit anti-myosin 7A (Proteus 25-6790), mouse anti-Yap (SC-101199), rabbit anti-Sall2 (HPA004162), and mouse anti-Pou4F3 (SC-81980)—were reconstituted in blocking solution and applied overnight at 4 ˚C.

Samples were washed with phosphate-buffered saline solution supplemented with 0.1 % Tween 20 (Sigma-Aldrich), after which Alexa Fluor-labeled secondary antisera (Life Technologies) were applied in the same solution for 1 hr at room temperature.

Nuclei were stained with 3 mM DAPI.

bioRxiv preprint doi: https://doi.org/10.1101/2020.02.11.944157; this version posted February 12, 2020. The copyright holder for this preprint (which was not certified by peer review) is the author/funder, who has granted bioRxiv a license to display the preprint in perpetuity. It is made available under aCC-BY-NC-ND 4.0 International license.

Immunofluorescence assays for cardiomyocytes

Cells were fixed in 4 % formaldehyde for 10 min with shaking at room temperature, permeabilized for 5 min with 0.5 % Triton X-100 in PBS, and blocked for 1 hr at room temperature with 5 % BSA in PBS containing 0.1% Triton X-100. The cells were labeled overnight at 4 ˚C with the primary antibodies anti-Ki67 (1:200, 275R, Cell Marque) and anti-phosphorylated histone 3 (1:200, 9701, Cell Signaling) for. After three washes with PBS, samples were labeled for 1 hr at room temperature with fluorescent secondary antibodies (Abcam) followed by 10 min of DAPI staining for nuclear visualization. After three washes in PBS, cells were imaged with a Nikon Eclipse Ti2 microscope.

Immunofluorescence imaging of retinal organoids

Fresh frozen sections were permeabilized and blocked in a humidified chamber for 1 hr at room temperature with 3 % horse serum in PBS with 0.3 % Triton X-100. The slides were exposed for 2 hr to primary antibodies diluted in the same solution. Anti-Sox-9 (1:100, Rb Cell Signaling 82630) was used to mark Müller cells. Slides were washed three times with PBS. Secondary antisera (Alexa-Fluor 488 and 647) diluted 1:10,000 in the serum solution were added for 1 hr at room temperature followed by two washes with PBS. Labeling for 30 min at room temperature (Apply Click-iT Invitrogen Alexa Fluor 555 C10338) was followed by a wash with PBS. After incubation with DAPI (1:10,000 in PBS) for 5 min and the application of mounting solution, sections were imaged by confocal microscopy with a Zeiss LSM 700 system with a 20X/0.8 NA objective lens with a pinhole size set at the first Airy disc.

Protein immunoblotting and quantification

MCF 10A, HEK293 cells, retinal organoids, and utricles were lysed on ice in radioimmunoprecipitation assay buffer solution (RIPA; BP-115-5x) with protease inhibitors (Halt Protease Inhibitor Cocktail, Thermo 87786). Utricles were additionally sonicated thrice at low power for 10 s, with breaks of 20 s with the samples kept on ice between sonications After lysates had been scraped and centrifuged at 10,000 RPM for 10 min at 4 ˚C, the supernatants were immediately subjected to electrophoresis or stored at -80 ˚C.

bioRxiv preprint doi: https://doi.org/10.1101/2020.02.11.944157; this version posted February 12, 2020. The copyright holder for this preprint (which was not certified by peer review) is the author/funder, who has granted bioRxiv a license to display the preprint in perpetuity. It is made available under aCC-BY-NC-ND 4.0 International license.

A standard immunoblotting protocol was used with the following specifications. A 4-12 % bis-tris gel (Thermo NP0322) was used to resolve the proteins in 5 mg of each sample. The proteins were transferred to a nitrocellulose membrane (BioRad 1704156) and blocked for 1 hr at room temperature (Rockland MB-070). After primary antibodies had been reconstituted in the same solution, the membrane was incubated overnight at 4 ˚C. After three 5 min washes at room temperature in tris-buffered saline solution with 0.05 % Tween 20, a secondary antibody conjugated to horseradish peroxidase (Millipore) was applied in the same solution for 1 hr at room temperature before activity was detected (SuperSignal West Pico PLUS, Thermo 34580). Images were acquired with an iBrightFL1000 system.

We used at a dilution of 1:1000 primary antibodies directed against Yap (sc-101199), phospho-Yap S127 (CST 4911), Lats1 and Lats2 (Abcam, ab70565), phospho-Lats1 S909 (CST 9157), Mst1 (CST 3682), Mob1 (CST 13730), phospho-Mob1 T35 (CST 8699), tubulin (Sigma T6793), and GAPDH(Abcam ab8245).

Cultured cardiomyocytes were lysed using RIPA supplemented with protease and phosphatase inhibitors (1:100, Sigma). Lysates were prepared and 30 μg protein of each sample was fractionated by gel electrophoresis in tris-glycine acrylamide gels, and subsequently transferred to a PVDF membrane. Following 1 hr blocking at room temperature, membranes were incubated with the following antibodies against phospho-Yap at s112 (1:1000, 13008, cell signaling), Yap (1:2000, NB110-58358, Novus) and Rabbit anti GAPDH (1:8000, PLA0125, Sigma) for 1 hr at room temperature. Following two washes in tris-buffered saline solution containing 0.1 % Tween 20, membranes were incubated with horseradish peroxidase anti-rabbit or secondary antibodies (Jackson). The signal was detected by super-signal west pico plus chemiluminescence kit (34580, Thermo-Fisher).

Immunoblots were quantified through measurement of band intensity with Fiji[59]. The final value of each band's intensity was normalized by the sum of all the bands' intensities. Significances from Student's *t*-tests are denoted as follows: *, $p < 0.05$; **, $p < 0.01$; ***, $p < 0.001$; ****, $p < 0.0001$. Unless otherwise indicated, error bars denote standard errors of means (SEMs).

bioRxiv preprint doi: https://doi.org/10.1101/2020.02.11.944157; this version posted February 12, 2020. The copyright holder for this preprint (which was not certified by peer review) is the author/funder, who has granted bioRxiv a license to display the preprint in perpetuity. It is made available under aCC-BY-NC-ND 4.0 International license.

Imaging of Yap nuclearization and quantification of proliferation

Confocal imaging was conducted with a confocal microscope enhanced with structured illumination (VT-iSIM, VisiTech International Ltd.).

For quantification of Yap nuclearization, for each condition two fields of supporting cells were imaged at 60X from two utricles. Using CellProlifer[60], we masked Sall2-positive nuclei and measured the intensity of their labeling. The same mask was then applied to the Yap channel and the intensity of labeling was measured. The ratio of the Yap to the Sall2 intensity was calculated for each condition in 680 cells after TRULI treatment and 570 cells for DMSO controls.

For quantifying the proliferation of supporting cells, we imaged utricles at 60X, then assembled the images into a composite tiling (Grid Collection Stitching, Fiji). The maximal values in *z*-stacks were projected to display the entire supporting-cell layer of the sensory epithelium, excluding connective tissue and the surrounding epithelium. Using CellProlifer[60], we counted the number of EdU-positive nuclei. Alternatively, EdU- and Sox2- doubly positive nuclei were counted using Multi-point Tool in ImageJ.

Images acquired from neonatal cardiac cultures were analyzed using ImageJ software by thresholding for cardiomyocytes according to endogenous tdTomato fluorescence. Thresholded figures were carefully and manually separated by fine lines to de-cluster cells in case they touch, basing on original images, following by measurements of area and solidity.

Images acquired from retina organoids were analyzed with CellProfiler[60]. Masks were created for all the Sox9-positive nuclei, and the percentage of EdU- and Sox9-positive nuclei were counted.

In vitro kinase assay

The *in vitro* kinase assay (HTRF KinEASE-STK S1, CisBio 62ST1PEB) was optimized to the linear reaction range of the enzymes Lats1 (Carna 01-123) and Lats2 (Carna 01-124). Reactions were conducted with 10 μM STK1 substrate and 10 μM ATP, unless otherwise indicated. For the ATP-shift assay, ATP was also used at concentrations of 50 μM and

bioRxiv preprint doi: https://doi.org/10.1101/2020.02.11.944157; this version posted February 12, 2020. The copyright holder for this preprint (which was not certified by peer review) is the author/funder, who has granted bioRxiv a license to display the preprint in perpetuity. It is made available under aCC-BY-NC-ND 4.0 International license.

250 μM. Lats1 was employed at a concentration of 200 pg/μL and Lats2 at 50 pg/μL, unless otherwise indicated. For the assay in which Michaelis-Menten constants for ATP were determined, each enzyme was at a concentration of 62.5 pg/uL, and Lats1 ran for 30 min, and the Lats2 ran for 20 min, all at room temperature. The DMSO concentration was maintained at 0.5 % (vol/vol) throughout all experiments, and a Janus 384 MDT (PerkinElmer) equipped with a 50 nL Pintool (V&P Scientific, Inc.) was used to add the compounds dissolved in DMSO to the reaction. The enzyme, substrate, ATP, and TRULI were combined in a low-volume 384-well plate and shaken for 50 min at room temperature, unless otherwise indicated. The reaction was stopped by adding the detection reagents, which were prepared at an 8:1 biotin:streptavidin ratio, and shaken for 60 min at room temperature. All reactions were conducted in triplicate and a Synergy NEO (Biotek) was used to detect the signal.

Cellular kinase assay

HEK293A cells were plated overnight in 96-well culture plates at a density of 50,000 cells per well in the medium described above. To start the assay, new serum-free medium with various concentrations of the compound was added to the cells, which were then incubated for 30 min at 37 ˚C. The DMSO concentration was kept at 0.1 % (vol/vol), and all experiments were performed in triplicate.

Total Yap and phospho-Yap were detected according to the two-plate protocol for adherent cells (Total Yap Cellular Kit, Cisbio 64YATPEG; phospho-Yap [Ser127] Cellular Kit, Cisbio 64YapPEG). The signal was detected by Synergy NEO (Biotek).

Modeling of enzyme structure

Lats1 and Lats2 are in the AGC kinase family, which also contains kinase sub-families such as Ndr and Rock[33]. In *Homo sapiens*, Lats1 has an overall sequence identity of 51.7% with Lats2, of 42.2% with Ndr2, and of 39.9% with Rock1. Owing to the presence of the classic kinase hinge-binding azaindole motif in TRULI, we focused on the kinase

bioRxiv preprint doi: https://doi.org/10.1101/2020.02.11.944157; this version posted February 12, 2020. The copyright holder for this preprint (which was not certified by peer review) is the author/funder, who has granted bioRxiv a license to display the preprint in perpetuity. It is made available under aCC-BY-NC-ND 4.0 International license.

domain and analyzed the ATP-binding site in order to generate a homology model. To define this site we used the 36 kinase-domain residues defined by Huang et al.[61]. We show an alignment of these ATP-binding site residues for 62 human AGC kinases (Table S1) and the identities of these residues between Lats and the other AGC kinases (Table S2). It is worth noting that the sequence identity between Lats1 and Lats2 in the ATP-binding site is 97.2%, with only a single conservative difference (lysine to arginine).

To generate a homology model of the kinase domain we selected a complex of Rock1 bound to an azaindole thiazole inhibitor (PDB ID: 5KKS)[62] . This complex was selected because the sequence identity between Lats1 and Rock1 in the ATP binding site is 72.2% and the bound inhibitor shares an azaindole group with TRULI. Athough the resolution of the structure is a modest 0.33 nm (3.3 Å), the electron density within the ATP-binding site is good and allows the conformation of the ligand and the amino acid side-chains to be determined unambiguously. The protein structure was downloaded from the Protein Databank, selenomethionines were changed to methionines, and missing sidechains were added with Schrodinger's Preparation Wizard. This program was also used to fix the orientations of the asparagine, glutamine, and histidine residues as well as the protonation states of all ionizable residues. Heteroatomic species such as water molecules, buffer solvents. and ions were removed and the complex was energy minimized with a restraint of the all-atom root-mean-square distance to 0.03 nm (0.3 Å). The homology model was generated from residues 705-1043 of Lats1 with a knowledge-based model in Schrodinger's Advanced Homology tool. Chain B of ROCK1 was used as the template and the azaindole thiazole inhibitor was retained.

The resulting homology model was then used for molecular docking with Schrodinger's Glide SP[63]. The Glide grid was generated around the azaindole thiazole inhibitor in the ATP-binding site with T845 as a rotatable group. TRULI was prepared using Schrodinger's Ligprep and docked using Schrodinger's Glide SP using default input parameters. The Glide SP docking score was -39 kJ/mol (-9.4 kcal/mol), corresponding to a binding affinity of approximately 130 nM.

The ligand's azaindole group is predicted to bind to the hinge region as expected, whereas the ligand's thiazolimine group contacts D846 in the DFG loop and the ligand's

bioRxiv preprint doi: https://doi.org/10.1101/2020.02.11.944157; this version posted February 12, 2020. The copyright holder for this preprint (which was not certified by peer review) is the author/funder, who has granted bioRxiv a license to display the preprint in perpetuity. It is made available under aCC-BY-NC-ND 4.0 International license.

benzyl group contacts the C-terminal F1039, which forms the active-site tether in many AGC kinases[64].

Although the numbers assigned to the amino-acid residues of various proteins elsewhere in the text refer to the murine products, those in the present paragraph reference the human proteins.

RNA sequencing and data analysis

Supporting cells were isolated by fluorescence-activated cell sorting from the utricles of *Lfng-EGFP* mice as described previously[65]. The total RNA was extracted using Quick-RNA MicroPrep kit (Zymo Research) and stored up to 2 weeks at -80 ˚C. RNA samples were then processed for library preparation with QIAseq FX Single Cell RNA Library Kit (Qiagen) and the quality of the library was confirmed using a Bioanalyzer (Quick Biology Inc.). A minimum of two biological replicates were collected for each condition, and at least 20 million 150 base-paired-end reads were sequenced for each replicate. Reads were mapped to GRCm38/mm10 genome assembly using STAR[66]. Differentially expressed genes were identified by DESeq2[67]. Only the protein coding sequences were considered for FPKM calculation. For data visualization, the ggplot2 package was used (H. Wickham, Springer New York, 2009). Principal components analysis was performed with pcaExplorer[68] on the 1000 genes whose differential expression was most significant.

Adenoviral gene transfer

The AdEasy Adenoviral Vector System (Agilent) was used to create adenoviral vectors containing the full-length coding sequence of murine Atoh1 under the control of a cytomegalovirus promoter. To permit the identification of infected cells, we also included sequences for an internal ribosome-entry site and for RFP. Viral particles were amplified and purified by CsCl-gradient centrifugation followed by dialysis (Viral Vector Core Facility, Sanford Burnham Prebys Medical Discovery Institute). Utricles were infected in 200 µL of culture medium with 10 µL of virus at a titer of 10^{10} pfu/mL. Ad-RFP virus (Vector Biolabs) at the same titer were used as a control.

bioRxiv preprint doi: https://doi.org/10.1101/2020.02.11.944157; this version posted February 12, 2020. The copyright holder for this preprint (which was not certified by peer review) is the author/funder, who has granted bioRxiv a license to display the preprint in perpetuity. It is made available under aCC-BY-NC-ND 4.0 International license.

Supplemental Information

Supplemental information can be found online at —.

Acknowledgments

This project was made possible by the dedicated personnel of two service facilities. At Rockefeller University's High-Throughput Screening Resource Center directed by Fraser Glickman, Carolina Adura Alcaino helped design assays for enzyme activity. The effort was supported in part by the Robertson Therapeutic Development Fund. At the Tri-Institutional Therapeutics Discovery Institute supervised by Peter Meinke, Leigh Baxt, Stacia Kargman, Robert Myers, and Nigel Liverton assisted with assay design and Rui Liang performed chemical syntheses. Masha Vologodskaia, Welly Makmura, Juan Llamas, Angela Ferrario, Rosanna Calderon, and Kayla Stepanian provided technical assistance. The pipeline for RNA sequencing data quality control and alignment was modified from EndCode by Litao Tao, Talon Trecek, and Francis James. We thank the members of our research groups for comments on the manuscript. NK was supported by the NIGMS (T32GM007739); KG by the NIDCD (R21DC016984); TA by the Studienstiftung des deutschen Volkes; AA, AS, and ET by European Research Council (ERC AdG 788194, CardHeal), the Israel Science Foundation (ISF), and the Foundations Leducq and Minerva; AN by Research to Prevent Blindness and the Las Madrinas Endowment in Experimental Therapeutics for Ophthalmology; and NS by the Hearing Restoration Program of the Hearing Health Foundation and the NIDCD (R01DC015829 and R01DC015530). AJH is an Investigator of Howard Hughes Medical Institute.

Author Contributions

Conceptualization, KG, AJH, and NK; Methodology, JC, DJH; Formal Analysis, KG and NK; Investigation: KG, NK, TA, AAP, JC, AA, and AS; Resources, ET, AN, NS, and AJH;

bioRxiv preprint doi: https://doi.org/10.1101/2020.02.11.944157; this version posted February 12, 2020. The copyright holder for this preprint (which was not certified by peer review) is the author/funder, who has granted bioRxiv a license to display the preprint in perpetuity. It is made available under aCC-BY-NC-ND 4.0 International license.

Writing – Original Draft, NK; Writing – Review and Editing, AJH, KG, NK, NS; Visualization, KG, NK, DJH, and AJH; Supervision, AJH; Funding Acquisition, ET, AN, NS, and AJH

Declaration of Interests

KG, NK, TA, AAP, and AJH are parties to an application for patent protection of derivatives of the Lats inhibitor presented here.

References

1. Moya, I. M. & Halder, G. Hippo-YAP/TAZ signalling in organ regeneration and regenerative medicine. *Nat. Rev. Mol. Cell Biol.* **20**, 211–226 (2019).
2. Meng, Z., Moroishi, T. & Guan, K.-L. Mechanisms of Hippo pathway regulation. *Genes Dev.* **30**, 1–17 (2016).
3. Johnson, R. & Halder, G. The two faces of Hippo: targeting the Hippo pathway for regenerative medicine and cancer treatment. *Nat. Rev. Drug Discov.* **13**, 63–79 (2013).
4. Silver, J., Schwab, M. E. & Popovich, P. G. Central Nervous System Regenerative Failure: Role of Oligodendrocytes, Astrocytes, and Microglia. *Cold Spring Harb. Perspect. Biol.* **7**, a020602 (2015).
5. Hashimoto, H., Olson, E. N. & Bassel-Duby, R. Therapeutic approaches for cardiac regeneration and repair. *Nat. Rev. Cardiol.* **15**, 585–600 (2018).
6. Burns, J. C. & Stone, J. S. Development and regeneration of vestibular hair cells in mammals. *Semin. Cell Dev. Biol.* **65**, 96–105 (2017).
7. Groves, A. K. The challenge of hair cell regeneration. *Exp. Biol. Med.* **235**, 434–446 (2010).

bioRxiv preprint doi: https://doi.org/10.1101/2020.02.11.944157; this version posted February 12, 2020. The copyright holder for this preprint (which was not certified by peer review) is the author/funder, who has granted bioRxiv a license to display the preprint in perpetuity. It is made available under aCC-BY-NC-ND 4.0 International license.

8. Scheibinger, M., Ellwanger, D. C., Corrales, C. E., Stone, J. S. & Heller, S. Aminoglycoside Damage and Hair Cell Regeneration in the Chicken Utricle. *J. Assoc. Res. Otolaryngol.* **19**, 17–29 (2018).
9. Kelley, M. W., Talreja, D. R. & Corwin, J. T. Replacement of hair cells after laser microbeam irradiation in cultured organs of corti from embryonic and neonatal mice. *J. Neurosci. Off. J. Soc. Neurosci.* **15**, 3013–3026 (1995).
10. Golub, J. S. *et al.* Hair Cell Replacement in Adult Mouse Utricles after Targeted Ablation of Hair Cells with Diphtheria Toxin. *J. Neurosci.* **32**, 15093–15105 (2012).
11. Burns, J. C., Cox, B. C., Thiede, B. R., Zuo, J. & Corwin, J. T. In vivo proliferative regeneration of balance hair cells in newborn mice. *J. Neurosci. Off. J. Soc. Neurosci.* **32**, 6570–6577 (2012).
12. Cox, B. C. *et al.* Spontaneous hair cell regeneration in the neonatal mouse cochlea in vivo. 15 (2014).
13. Totaro, A., Panciera, T. & Piccolo, S. YAP/TAZ upstream signals and downstream responses. *Nat. Cell Biol.* **20**, 888–899 (2018).
14. Morikawa, Y., Heallen, T., Leach, J., Xiao, Y. & Martin, J. F. Dystrophin-glycoprotein complex sequesters Yap to inhibit cardiomyocyte proliferation. *Nature* **547**, 227–231 (2017).
15. Bassat, E. *et al.* The extracellular matrix protein agrin promotes heart regeneration in mice. *Nature* **547**, 179–184 (2017).
16. Monroe, T. O. *et al.* YAP Partially Reprograms Chromatin Accessibility to Directly Induce Adult Cardiogenesis In Vivo. *Dev. Cell* **48**, 765-779.e7 (2019).
17. Rueda, E. M. *et al.* The Hippo Pathway Blocks Mammalian Retinal Müller Glial Cell Reprogramming. *Cell Rep.* **27**, 1637-1649.e6 (2019).
18. Fan, F. *et al.* Pharmacological targeting of kinases MST1 and MST2 augments tissue repair and regeneration. *Sci. Transl. Med.* **8**, 352ra108–352ra108 (2016).

bioRxiv preprint doi: https://doi.org/10.1101/2020.02.11.944157; this version posted February 12, 2020. The copyright holder for this preprint (which was not certified by peer review) is the author/funder, who has granted bioRxiv a license to display the preprint in perpetuity. It is made available under aCC-BY-NC-ND 4.0 International license.

19. Gnedeva, K., Jacobo, A., Salvi, J. D., Petelski, A. A. & Hudspeth, A. J. Elastic force restricts growth of the murine utricle. *eLife* **6**, (2017).
20. Kim, N.-G., Koh, E., Chen, X. & Gumbiner, B. M. E-cadherin mediates contact inhibition of proliferation through Hippo signaling-pathway components. *Proc. Natl. Acad. Sci. U. S. A.* **108**, 11930–11935 (2011).
21. Schlegelmilch, K. *et al.* Yap1 acts downstream of α-catenin to control epidermal proliferation. *Cell* **144**, 782–795 (2011).
22. Zhao, B. *et al.* Inactivation of YAP oncoprotein by the Hippo pathway is involved in cell contact inhibition and tissue growth control. *Genes Dev.* **21**, 2747–2761 (2007).
23. Mellado Lagarde, M. M. *et al.* Spontaneous regeneration of cochlear supporting cells after neonatal ablation ensures hearing in the adult mouse. *Proc. Natl. Acad. Sci.* **111**, 16919–16924 (2014).
24. Xu, J. *et al.* Identification of mouse cochlear progenitors that develop hair and supporting cells in the organ of Corti. *Nat. Commun.* **8**, 15046 (2017).
25. Liu-Chittenden, Y. *et al.* Genetic and pharmacological disruption of the TEAD-YAP complex suppresses the oncogenic activity of YAP. *Genes Dev.* **26**, 1300–1305 (2012).
26. Zhang, N. *et al.* The Merlin/NF2 tumor suppressor functions through the YAP oncoprotein to regulate tissue homeostasis in mammals. *Dev. Cell* **19**, 27–38 (2010).
27. Arnold, K. *et al.* Sox2(+) adult stem and progenitor cells are important for tissue regeneration and survival of mice. *Cell Stem Cell* **9**, 317–329 (2011).
28. Huang, W. *et al.* The N-terminal phosphodegron targets TAZ/WWTR1 protein for SCFβ-TrCP-dependent degradation in response to phosphatidylinositol 3-kinase inhibition. *J. Biol. Chem.* **287**, 26245–26253 (2012).
29. Mo, J.-S. *et al.* Cellular energy stress induces AMPK-mediated regulation of YAP and the Hippo pathway. *Nat. Cell Biol.* **17**, 500–510 (2015).

bioRxiv preprint doi: https://doi.org/10.1101/2020.02.11.944157; this version posted February 12, 2020. The copyright holder for this preprint (which was not certified by peer review) is the author/funder, who has granted bioRxiv a license to display the preprint in perpetuity. It is made available under aCC-BY-NC-ND 4.0 International license.

30. Hong, A. W. & Guan, K.-L. Non-radioactive LATS in vitro Kinase Assay. *Bio-Protoc.* **7**, (2017).

31. Moroishi, T. *et al.* A YAP/TAZ-induced feedback mechanism regulates Hippo pathway homeostasis. *Genes Dev.* **29**, 1271–1284 (2015).

32. https://www.cisbio.com/media/asset/l/s/ls-tn-lats1.pdf.

33. Pearce, L. R., Komander, D. & Alessi, D. R. The nuts and bolts of AGC protein kinases. *Nat. Rev. Mol. Cell Biol.* **11**, 9–22 (2010).

34. Hirozane, Y. *et al.* Structure-based rational design of staurosporine-based fluorescent probe with broad-ranging kinase affinity for kinase panel application. *Bioorg. Med. Chem. Lett.* **29**, 126641 (2019).

35. http://www.reactionbiology.com/webapps/site/kinaseassay.aspx?gclid=EAIaIQobChMI9K2248-V5wIVyp6zCh2HSwAKEAAYASABEgJCsPD_BwE.

36. Heintz, N. Gene expression nervous system atlas (GENSAT). *Nat. Neurosci.* **7**, 483 (2004).

37. Huang, D. W., Sherman, B. T. & Lempicki, R. A. Systematic and integrative analysis of large gene lists using DAVID bioinformatics resources. *Nat. Protoc.* **4**, 44–57 (2009).

38. Burns, J. C., On, D., Baker, W., Collado, M. S. & Corwin, J. T. Over half the hair cells in the mouse utricle first appear after birth, with significant numbers originating from early postnatal mitotic production in peripheral and striolar growth zones. *J. Assoc. Res. Otolaryngol. JARO* **13**, 609–627 (2012).

39. Gnedeva, K. & Hudspeth, A. J. SoxC transcription factors are essential for the development of the inner ear. *Proc. Natl. Acad. Sci.* **112**, 14066–14071 (2015).

40. Zanconato, F. *et al.* Genome-wide association between YAP/TAZ/TEAD and AP-1 at enhancers drives oncogenic growth. *Nat. Cell Biol.* **17**, 1218–1227 (2015).

bioRxiv preprint doi: https://doi.org/10.1101/2020.02.11.944157; this version posted February 12, 2020. The copyright holder for this preprint (which was not certified by peer review) is the author/funder, who has granted bioRxiv a license to display the preprint in perpetuity. It is made available under aCC-BY-NC-ND 4.0 International license.

41. Gnedeva, K., Jacobo, A., Salvi, J. D., Petelski, A. A. & Hudspeth, A. J. Elastic force restricts growth of the murine utricle. *eLife* **6**, (2017).

42. Frade, J. M. & Ovejero-Benito, M. C. Neuronal cell cycle: the neuron itself and its circumstances. *Cell Cycle Georget. Tex* **14**, 712–720 (2015).

43. Morikawa, Y. *et al.* Actin cytoskeletal remodeling with protrusion formation is essential for heart regeneration in Hippo-deficient mice. *Sci. Signal.* **8**, ra41–ra41 (2015).

44. Yao, K. *et al.* Restoration of vision after de novo genesis of rod photoreceptors in mammalian retinas. *Nature* **560**, 484–488 (2018).

45. Meng, Z. *et al.* MAP4K family kinases act in parallel to MST1/2 to activate LATS1/2 in the Hippo pathway. *Nat. Commun.* **6**, 247 (2015).

46. Lee, Y.-S., Liu, F. & Segil, N. A morphogenetic wave of p27Kip1 transcription directs cell cycle exit during organ of Corti development. *Dev. Camb. Engl.* **133**, 2817–2826 (2006).

47. Chai, R. *et al.* Wnt signaling induces proliferation of sensory precursors in the postnatal mouse cochlea. *Proc. Natl. Acad. Sci. U. S. A.* **109**, 8167–8172 (2012).

48. Jacques, B. E. *et al.* A dual function for canonical Wnt/β-catenin signaling in the developing mammalian cochlea. *Dev. Camb. Engl.* **139**, 4395–4404 (2012).

49. Shi, F., Hu, L. & Edge, A. S. B. Generation of hair cells in neonatal mice by β-catenin overexpression in Lgr5-positive cochlear progenitors. *Proc. Natl. Acad. Sci. U. S. A.* **110**, 13851–13856 (2013).

50. Ni, W. *et al.* Extensive Supporting Cell Proliferation and Mitotic Hair Cell Generation by In Vivo Genetic Reprogramming in the Neonatal Mouse Cochlea. *J. Neurosci. Off. J. Soc. Neurosci.* **36**, 8734–8745 (2016).

51. Furth, N. & Aylon, Y. The LATS1 and LATS2 tumor suppressors: beyond the Hippo pathway. *Cell Death Differ.* **24**, 1488–1501 (2017).

52. Juan, W. & Hong, W. Targeting the Hippo Signaling Pathway for Tissue Regeneration and Cancer Therapy. *Genes* **7**, 55 (2016).

bioRxiv preprint doi: https://doi.org/10.1101/2020.02.11.944157; this version posted February 12, 2020. The copyright holder for this preprint (which was not certified by peer review) is the author/funder, who has granted bioRxiv a license to display the preprint in perpetuity. It is made available under aCC-BY-NC-ND 4.0 International license.

53. Moroishi, T. *et al.* The Hippo Pathway Kinases LATS1/2 Suppress Cancer Immunity. *Cell* **167**, 1525–1539.e17 (2016).

54. Agah, R. *et al.* Gene recombination in postmitotic cells. Targeted expression of Cre recombinase provokes cardiac-restricted, site-specific rearrangement in adult ventricular muscle in vivo. *J. Clin. Invest.* **100**, 169–179 (1997).

55. Madisen, L. *et al.* A robust and high-throughput Cre reporting and characterization system for the whole mouse brain. *Nat. Neurosci.* **13**, 133–140 (2010).

56. Bickerton, G. R., Paolini, G. V., Besnard, J., Muresan, S. & Hopkins, A. L. Quantifying the chemical beauty of drugs. *Nat. Chem.* **4**, 90–98 (2012).

57. Gnedeva, K. & Hudspeth, A. J. SoxC transcription factors are essential for the development of the inner ear. *Proc. Natl. Acad. Sci.* **112**, 14066–14071 (2015).

58. Zhong, X. *et al.* Generation of three-dimensional retinal tissue with functional photoreceptors from human iPSCs. *Nat. Commun.* **5**, 4047 (2014).

59. Schindelin, J. *et al.* Fiji: an open-source platform for biological-image analysis. *Nat. Methods* **9**, 676–682 (2012).

60. Carpenter, A. E. *et al.* CellProfiler: image analysis software for identifying and quantifying cell phenotypes. *Genome Biol.* **7**, R100 (2006).

61. Huang, D., Zhou, T., Lafleur, K., Nevado, C. & Caflisch, A. Kinase selectivity potential for inhibitors targeting the ATP binding site: a network analysis. *Bioinforma. Oxf. Engl.* **26**, 198–204 (2010).

62. Bandarage, U. K. *et al.* ROCK inhibitors 3: Design, synthesis and structure-activity relationships of 7-azaindole-based Rho kinase (ROCK) inhibitors. *Bioorg. Med. Chem. Lett.* **28**, 2622–2626 (2018).

63. Halgren, T. A. *et al.* Glide: a new approach for rapid, accurate docking and scoring. 2. Enrichment factors in database screening. *J. Med. Chem.* **47**, 1750–1759 (2004).

bioRxiv preprint doi: https://doi.org/10.1101/2020.02.11.944157; this version posted February 12, 2020. The copyright holder for this preprint (which was not certified by peer review) is the author/funder, who has granted bioRxiv a license to display the preprint in perpetuity. It is made available under aCC-BY-NC-ND 4.0 International license.

64. Kannan, N., Haste, N., Taylor, S. S. & Neuwald, A. F. The hallmark of AGC kinase functional divergence is its C-terminal tail, a cis-acting regulatory module. *Proc. Natl. Acad. Sci. U. S. A.* **104**, 1272–1277 (2007).

65. Burns, J. C., Kelly, M. C., Hoa, M., Morell, R. J. & Kelley, M. W. Single-cell RNA-Seq resolves cellular complexity in sensory organs from the neonatal inner ear. *Nat. Commun.* **6**, 8557 (2015).

66. Dobin, A. *et al.* STAR: ultrafast universal RNA-seq aligner. *Bioinforma. Oxf. Engl.* **29**, 15–21 (2013).

67. Love, M. I., Huber, W. & Anders, S. Moderated estimation of fold change and dispersion for RNA-seq data with DESeq2. *Genome Biol.* **15**, 550 (2014).

68. Marini, F. & Binder, H. pcaExplorer: an R/Bioconductor package for interacting with RNA-seq principal components. *BMC Bioinformatics* **20**, 331 (2019).

bioRxiv preprint doi: https://doi.org/10.1101/2020.02.11.944157; this version posted February 12, 2020. The copyright holder for this preprint (which was not certified by peer review) is the author/funder, who has granted bioRxiv a license to display the preprint in perpetuity. It is made available under aCC-BY-NC-ND 4.0 International license.

Figure Legends

Figure 1. High-throughput screen for activators of Yap translocation to nuclei

(A) A schematic diagram demonstrates the strategy for identification of compounds that promote the nuclear transit of Yap, thus reversing the exclusion characteristic of contact inhibition. (B) The number of MCF 10A cells rises almost linearly with their confluency. (C) Nuclear localization of Yap falls systematically with increasing confluency in MCF 10A cultures. (D) Immunolabeling of Yap (red) demonstrates nuclear localization of the protein in a positive-control (subconfluent) culture and in a negative-control (confluent) culture. Treatment of a confluent culture with a representative hit compound promotes extensive movement of Yap into nuclei.

See also Figure S1.

Figure 2. Activation of Yap and proliferation of supporting cells

(A) A timeline depicts the pattern of the experiments shown in the indicated subsequent panels. Treatment with TRULI is initiated at the outset. (B) TRULI exposure drives Yap into the nuclei of utricular supporting cells. (C) *In vitro* exposure to TRULI for 5 d elicits proliferation of supporting cells, as measured by the incorporation of EdU. Verteporfin, an inhibitor of the Yap-Tead interaction, drastically reduces this effect. (D) The nuclear localization of Yap is quantified as a ratio to the constitutively expressed protein Sall2 ($p < 0.0001$ by an unpaired, two-tailed *t*-test, $n = 570$ control nuclei and 680 treated nuclei). (E) The number of EdU-positive cells per utricle increases with TRULI ($p = 0.021$ by an unpaired, one-tailed *t*-test, control $n = 2$, TRULI $n = 3$), but the effect is blocked by verteporfin ($p = 0.028$ by an unpaired, one-tailed *t*-test, $n = 2$). (F) Conditional deletion of Yap by tamoxifen administration to *SOX2-Cre*^{ER} *Yap*$^{fl/fl}$ (Yap CKO) animals at P1, 7 d or 14 d prior to explantation, decreases the number of Sox2 (red) and EdU (white) doubly positive supporting cells compared to Cre-negative *Yap*$^{fl/fl}$ (WT) littermates. (G) Quantification of the number of EdU-positive cells in panel F demonstrates that

bioRxiv preprint doi: https://doi.org/10.1101/2020.02.11.944157; this version posted February 12, 2020. The copyright holder for this preprint (which was not certified by peer review) is the author/funder, who has granted bioRxiv a license to display the preprint in perpetuity. It is made available under aCC-BY-NC-ND 4.0 International license.

decrease in supporting-cell proliferation is statistically significant (Student's *t*-tests; $n = 3$ for wild-type control and Yap CKO at 7 d; $n = 4$ for TRULI treatment; $n = 6$ for Yap CKO at 10 d and TRULI).

See also Figure S2.

Figure 3. ATP-competitive inhibition of Lats kinases.

(A) Protein immunoblotting discloses that treatment of MCF 10A cells with TRULI leaves Hippo signaling intact through the activation of Lats kinases, but that Yap phosphorylation is greatly diminished. (B) Serum starvation of HEK293A cells in the presence of TRULI also demonstrates Lats activation but suppression of Yap phosphorylation. (C) TRULI comprises a thiazolimine backbone with two substituents: a benzyl group and a 7-azaindole hinge-binding motif. (D) In a simulated structure of TRULI in the predicted ATP-binding site of Lats1, the protein is displayed as a ribbon with heavy atoms in atom-colored wire representation with grey carbons. TRULI is displayed in an atom-colored, ball-and-stick representation. Aspartate 846 is positioned to bind the thiazolimine group and phenylalanine 1039 to interact with the benzyl moiety. (E) An *in vitro* assay of Lats1 kinase activity shows that the IC_{50} for TRULI increases with the ATP concentration, from 0.2 nM at 10 μM, to 4.3 nM at 50 μM, and to 80 nM at 250 μM, demonstrating that the compound is an ATP-competitive inhibitor. (F) A kinase assay conducted with serum-starved HEK293A cells indicates an EC_{50} of 510 nM for TRULI. Starvation does not significantly deplete the total amount of Yap. In panels E and F, error bars represent SEs.

See also Figures S3 and S4.

Figure 4. Gene-expression changes evoked treatment in supporting cells by TRULI.

(A) For three experiments, principal-component analysis was performed on RNA-sequencing data obtained from supporting cells after 5 d of treatment with TRULI or from control samples. (B) A volcano plot visualizes the differentially expressed genes ($|\log_2(\text{fold change})| > 1$; padj<0.05). Genes upregulated after TRULI treatment compared

bioRxiv preprint doi: https://doi.org/10.1101/2020.02.11.944157; this version posted February 12, 2020. The copyright holder for this preprint (which was not certified by peer review) is the author/funder, who has granted bioRxiv a license to display the preprint in perpetuity. It is made available under aCC-BY-NC-ND 4.0 International license.

to control are labeled in red and those downregulated in blue. (C) Gene-ontology (GO) analysis performed with DAVID software demonstrates that the terms associated with the cell cycle are the most enriched in the genes upregulated by TRULI, whereas the terms associated with stress are more enriched in the control gene set. A full list of differentially expressed genes identified using DEseq2 is available on request. (D) For three experiments, a heatmap demonstrates the relative expression levels of 140 cell-cycle genes differentially expressed between control and TRULI-treated supporting cells (false discovery rate < 0.01) in comparison to E17.5. Highly expressed genes are shown in red and genes with relatively low levels of expression are depicted in blue. (E) Cell-cycle genes of the G1-S transition of the cell cycle are significantly upregulated by TRULI to the levels found in E17.5 supporting cells ($p < 0.001$ by a Wilcoxon signed-rank test). (F) Markers of the G2-M transition are likewise upregulated ($p < 0.001$ by a Wilcoxon signed-rank test). (G) For three experiments, the heatmap demonstrates the relative expression levels of 79 Yap-target genes differentially expressed between control and TRULI-treated supporting cells (false discovery rate < 0.01) in comparison to E17.5 embryonic levels. (H) The expression of Yap-target genes is upregulated in response to TRULI to the levels found in E17.5 supporting cells ($p < 0.05$ by a Wilcoxon signed-rank test). (I) In contrast, the relative level of expression for genes associated with cell death remains unchanged between controls, TRULI-treated, and E17.5 supporting cells ($p > 0.05$ by a Wilcoxon signed-rank test).

See also Figure S5.

Figure 5. Supporting-cell plasticity after TRULI treatment.

(A) A volcano plot visualizes the genes differentially expressed after 5 d of TRULI treatment followed by 5 d drug withdrawal ($|\log_2(\text{fold change})| > 1$; padj < 0.05). The subset of hair-cell genes most upregulated after TRULI treatment compared to control are labeled. (B) Gene-ontology analysis performed with DAVID software demonstrates

bioRxiv preprint doi: https://doi.org/10.1101/2020.02.11.944157; this version posted February 12, 2020. The copyright holder for this preprint (which was not certified by peer review) is the author/funder, who has granted bioRxiv a license to display the preprint in perpetuity. It is made available under aCC-BY-NC-ND 4.0 International license.

that the terms associated with hair-cell differentiation and function are the most enriched in the genes upregulated by TRULI. A full list of differentially expressed genes identified using DEseq2 is available on request. (C) In the representative examples of whole mount utricular explants after 5 d of TRULI treatment followed by 5 d drug withdrawal, immunolabeling for Pou4f3 (green) and Myo7a (red) depicts hair cells. New sensory receptors formed from proliferated supporting cells are identified by EdU-incorporation (white) and are found only after TRULI treatment. Nuclei are labeled with DAPI. (D) The total number of hair cells per utricle does not change after TRULI treatment ($p > 0.05$ by a Student's *t*-test; $n = 4$ for controls and $n = 5$ for TRULI treated animals).

See also Figure S6.

Figure 6. Proliferation of cardiomyocytes and Müller cells.

(A) A protein immunoblot indicates that TRULI decreases the phosphorylation of Yap in neonatal cardiomyocytes *in vitro*. (B) Quantification of the data in panel A shows the significance of the effect ($p = 0.008$ by an unpaired, two-tailed *t*-test, $n = 4$). (C) Immunofluorescent labeling discloses that 3 d of TRULI treatment elevates the cell-cycle marker Ki67 (arrowheads) in cardiomyocytes. Scale bars, 50 μm. (D) Quantification again reveals significant effects for Ki67 ($p = 0.001$ by an unpaired, two-tailed *t*-test, $n = 4$). (E) A marker of mitotic initiation, pH3, is similarly elevated by treatment ($p = 0.026$ by an unpaired, two-tailed *t*-test, $n = 4$). (F) The cardiomyocyte solidity, an index of cellular shape, decreases significantly after treatment, an effect consistent with de-differentiation ($p < 0.0001$ by an unpaired, two-tailed *t*-test, $n = 232$ control cells and 197 TRULI-treated cells). (G) TRULI treatment reduces the areas of cardiomyocytes, another sign of mitosis ($p < 0.0001$ by an unpaired, two-tailed *t*-test, $n = 231$ control cells and 197 TRULI-treated cells). (H) A protein immunoblot indicates that 24 hr of treatment with TRULI decreases the phosphorylation of Yap in Sox9-marked Müller cells of human retinal organoids. (I) A bar graph documents the effect observed in panel H ($p = 0.024$ by

bioRxiv preprint doi: https://doi.org/10.1101/2020.02.11.944157; this version posted February 12, 2020. The copyright holder for this preprint (which was not certified by peer review) is the author/funder, who has granted bioRxiv a license to display the preprint in perpetuity. It is made available under aCC-BY-NC-ND 4.0 International license.

an unpaired, two-tailed *t*-test, $n = 3$). (J) After 5 d of TRULI treatment, EdU labeling shows a substantial increase in cellular proliferation. (K) A bar graph quantifies the result of panel J in three experiments ($p < 0.0001$ by an unpaired, two-tailed *t*-test, $n = 15$ control organoids and 16 TRULI-treated organoids).

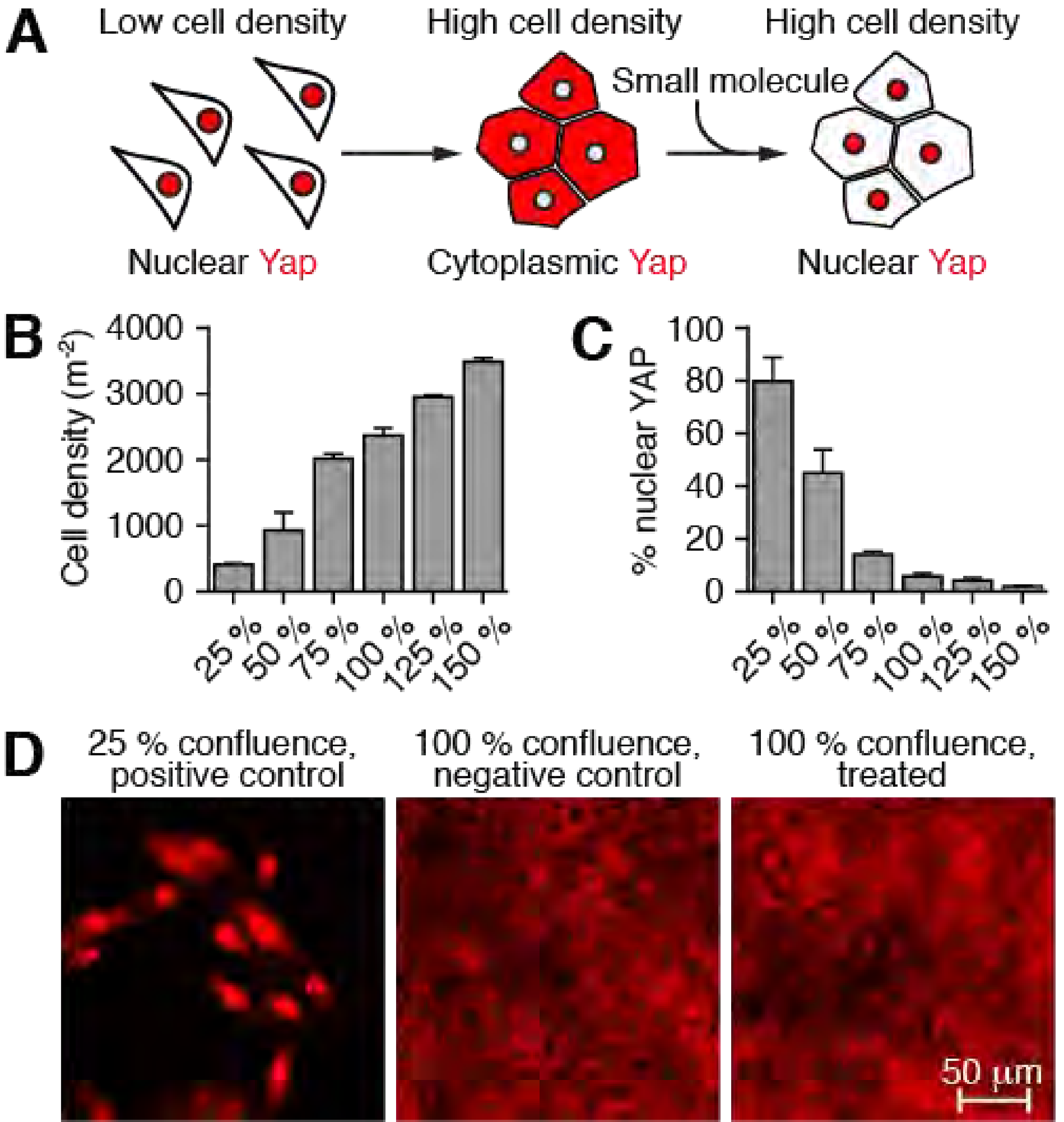
A
Low cell density
High cell density
High cell density
Small molecule
Nuclear Yap
Cytoplasmic Yap
Nuclear Yap
B
Cell density (m-2)
4000
3000
2000
1000
0
25 %
50 %
75 %
100 %
125 %
150 %
C
% nuclear YAP
100
80
60
40
20
0
25 %
50 %
75 %
100 %
125 %
150 %
D
25 % confluence, positive control
100 % confluence, negative control
100 % confluence, treated
50 µm

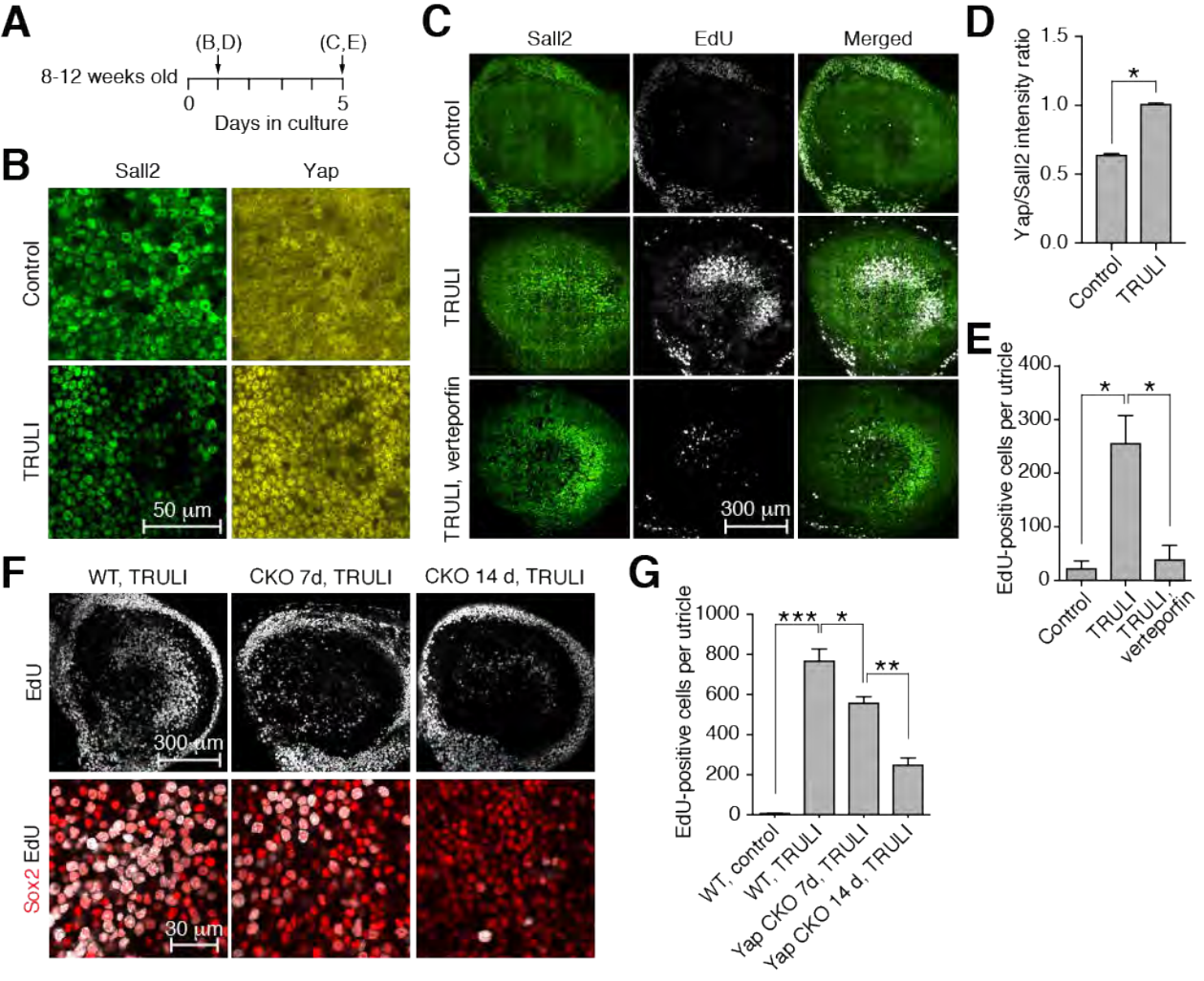
A
(B,D)
(C,E)
8-12 weeks old
0
5
Days in culture
B
Sall2
Yap
Control
TRULI
50 µm
C
Sall2
EdU
Merged
Control
TRULI
TRULI, verteporfin
300 µm
D
Yap/Sall2 intensity ratio
1.5
1.0
0.5
0.0
*
Control
TRULI
E
EdU-positive cells per utricle
400
300
200
100
0
*
*
Control
TRULI
TRULI, verteporfin
F
WT, TRULI
CKO 7d, TRULI
CKO 14 d, TRULI
EdU
300 µm
Sox2 EdU
30 µm
G
EdU-positive cells per utricle
1000
800
600
400
200
0
***
*
**
WT, control
WT, TRULI
Yap CKO 7d, TRULI
Yap CKO 14 d, TRULI

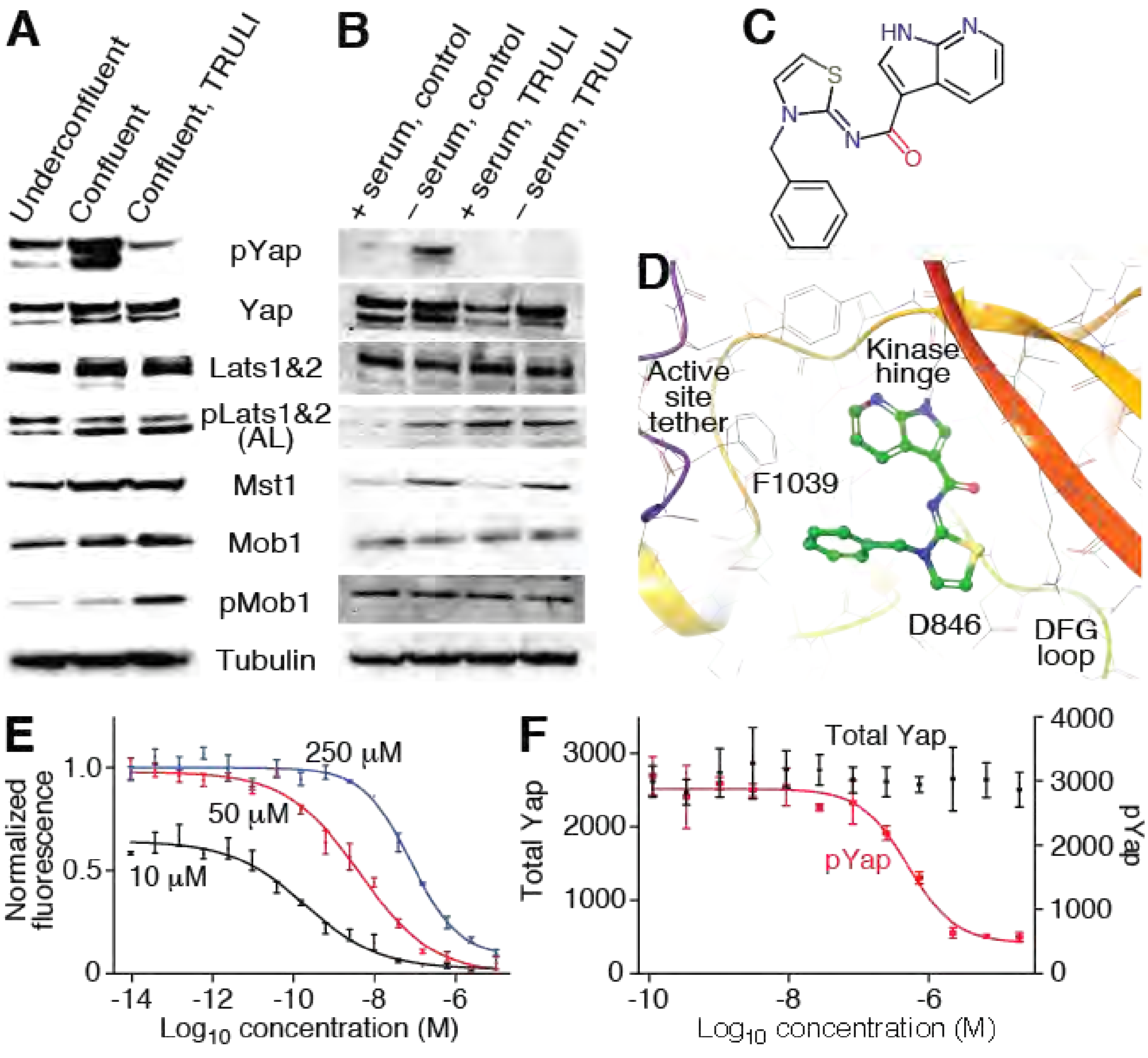
A
Underconfluent
Confluent
Confluent, TRULI
pYap
Yap
Lats1&2
pLats1&2 (AL)
Mst1
Mob1
pMob1
Tubulin
B
+ serum, control
– serum, control
+ serum, TRULI
– serum, TRULI
C
HN
N
S
N
N
O
D
Active site tether
Kinase hinge
F1039
D846
DFG loop
E
250 μM
50 μM
10 μM
Normalized fluorescence
1.0
0.5
0
-14
-12
-10
-8
-6
Log10 concentration (M)
F
Total Yap
pYap
Total Yap
pYap
3000
2000
1000
0
4000
3000
2000
1000
0
-10
-8
-6
Log10 concentration (M)

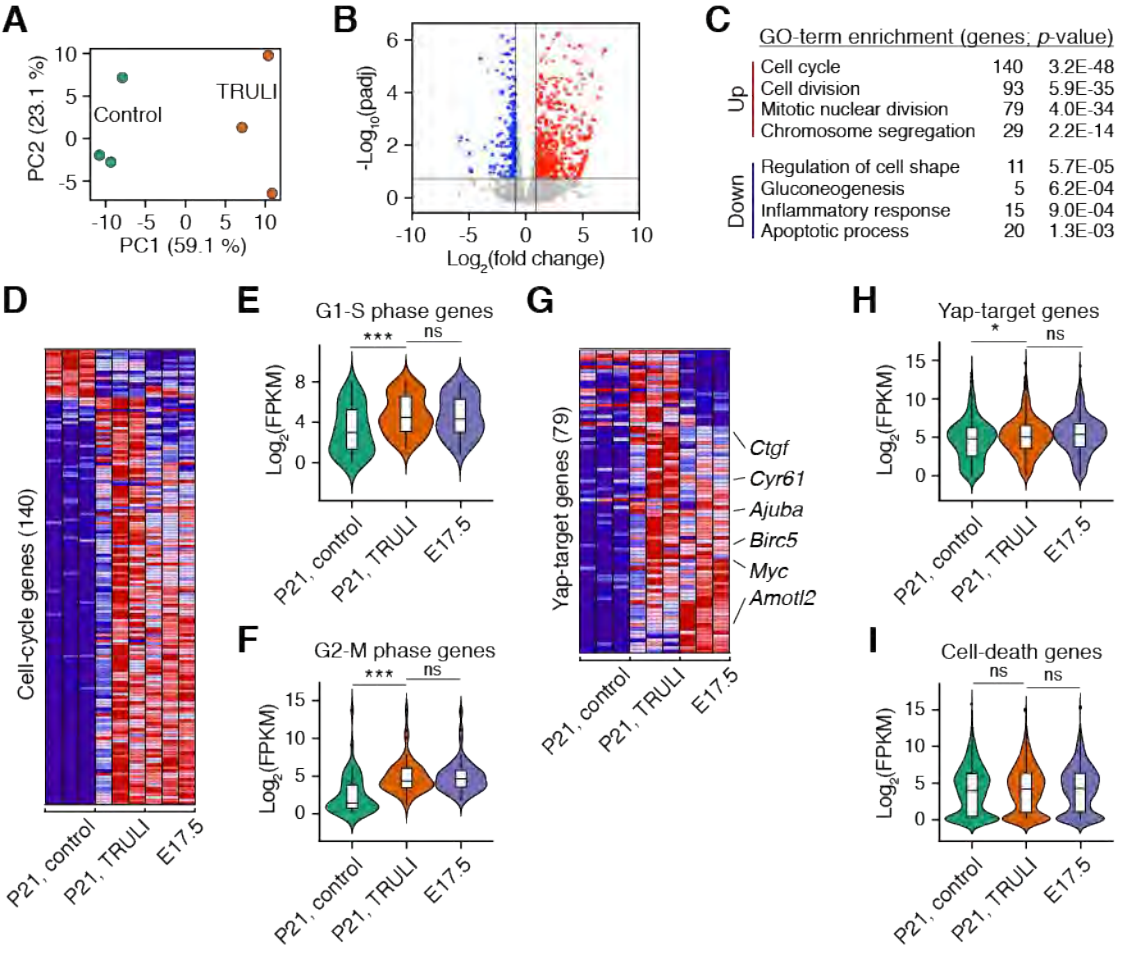
A
PC2 (23.1 %)
PC1 (59.1 %)
Control
TRULI
B
-Log10(padj)
Log2(fold change)
C
GO-term enrichment (genes; p-value)
Up
Cell cycle 140 3.2E-48
Cell division 93 5.9E-35
Mitotic nuclear division 79 4.0E-34
Chromosome segregation 29 2.2E-14
Down
Regulation of cell shape 11 5.7E-05
Gluconeogenesis 5 6.2E-04
Inflammatory response 15 9.0E-04
Apoptotic process 20 1.3E-03
D
Cell-cycle genes (140)
P21, control
P21, TRULI
E17.5
E
G1-S phase genes
Log2(FPKM)
***
ns
F
G2-M phase genes
G
Yap-target genes (79)
Ctgf
Cyr61
Ajuba
Birc5
Myc
Amotl2
H
Yap-target genes
*
I
Cell-death genes

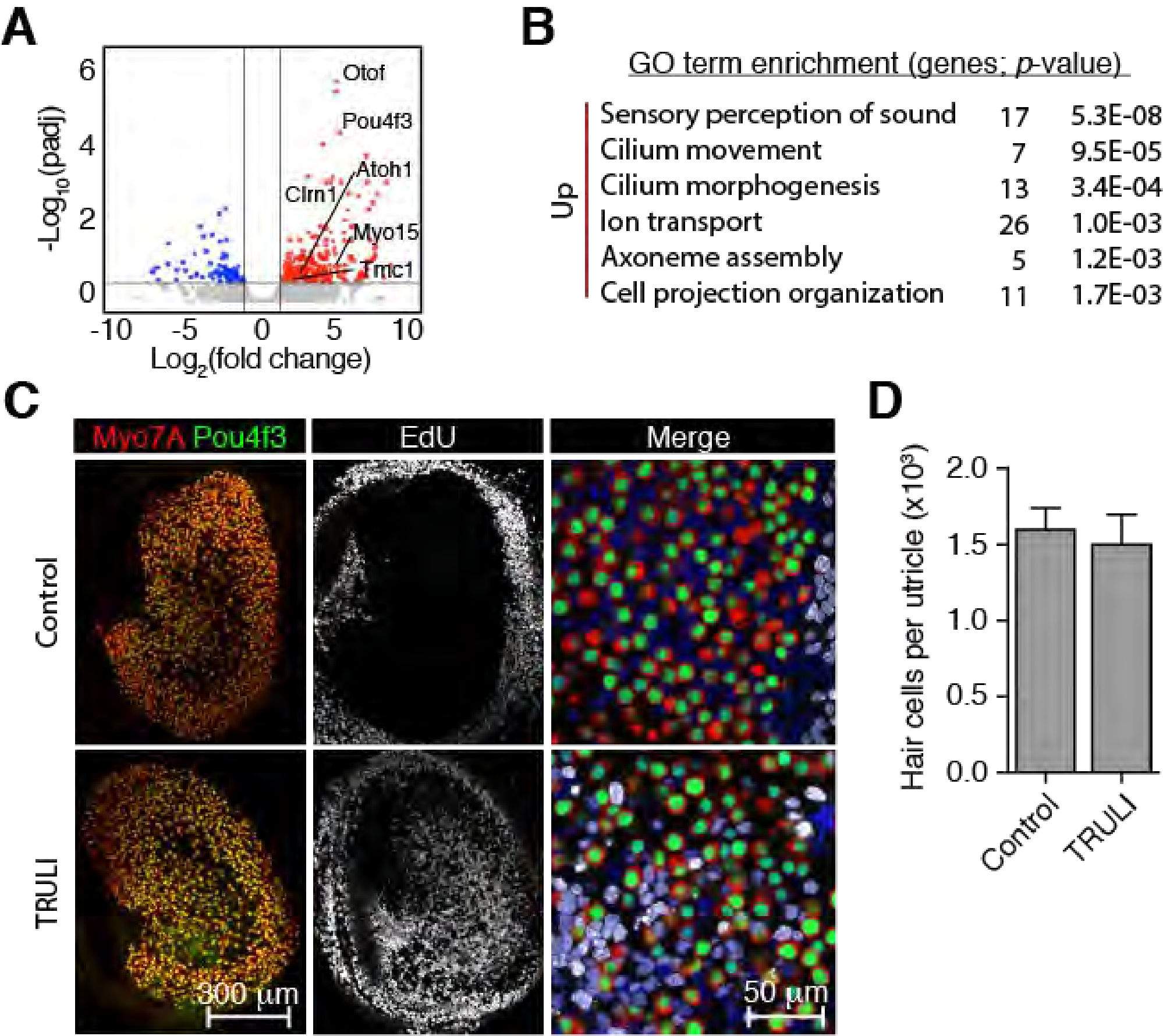
A
Otof
Pou4f3
Atoh1
Clrn1
Myo15
Tmc1
-Log10(padj)
Log2(fold change)
B
GO term enrichment (genes; p-value)
Up
Sensory perception of sound 17 5.3E-08
Cilium movement 7 9.5E-05
Cilium morphogenesis 13 3.4E-04
Ion transport 26 1.0E-03
Axoneme assembly 5 1.2E-03
Cell projection organization 11 1.7E-03
C
Myo7A Pou4f3
EdU
Merge
Control
TRULI
300 µm
50 µm
D
Hair cells per utricle (x10³)
Control
TRULI

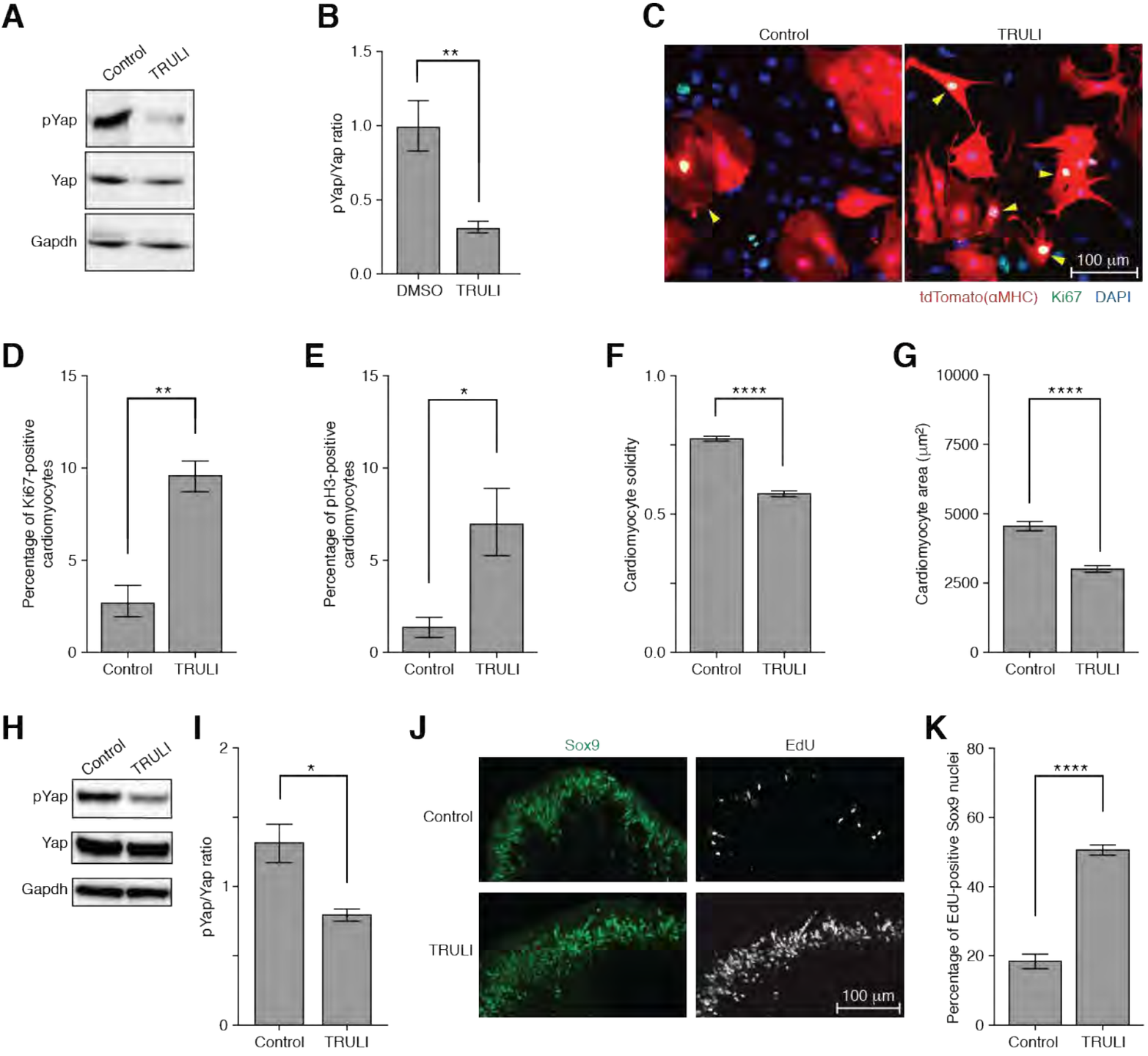
A
Control
TRULI
pYap
Yap
Gapdh
B
pYap/Yap ratio
1.5
1.0
0.5
0.0
**
DMSO
TRULI
C
Control
TRULI
100 μm
tdTomato(αMHC) Ki67 DAPI
D
Percentage of Ki67-positive cardiomyocytes
15
10
5
0
**
Control
TRULI
E
Percentage of pH3-positive cardiomyocytes
15
10
5
0
*
Control
TRULI
F
Cardiomyocyte solidity
1.0
0.5
0.0
****
Control
TRULI
G
Cardiomyocyte area (μm²)
10000
7500
5000
2500
0
****
Control
TRULI
H
Control
TRULI
pYap
Yap
Gapdh
I
pYap/Yap ratio
2
1
0
*
Control
TRULI
J
Sox9
EdU
Control
TRULI
100 μm
K
Percentage of EdU-positive Sox9 nuclei
80
60
40
20
0
****
Control
TRULI

bioRxiv preprint doi: https://doi.org/10.1101/2020.02.11.944157; this version posted February 12, 2020. The copyright holder for this preprint (which was not certified by peer review) is the author/funder, who has granted bioRxiv a license to display the preprint in perpetuity. It is made available under aCC-BY-NC-ND 4.0 International license.

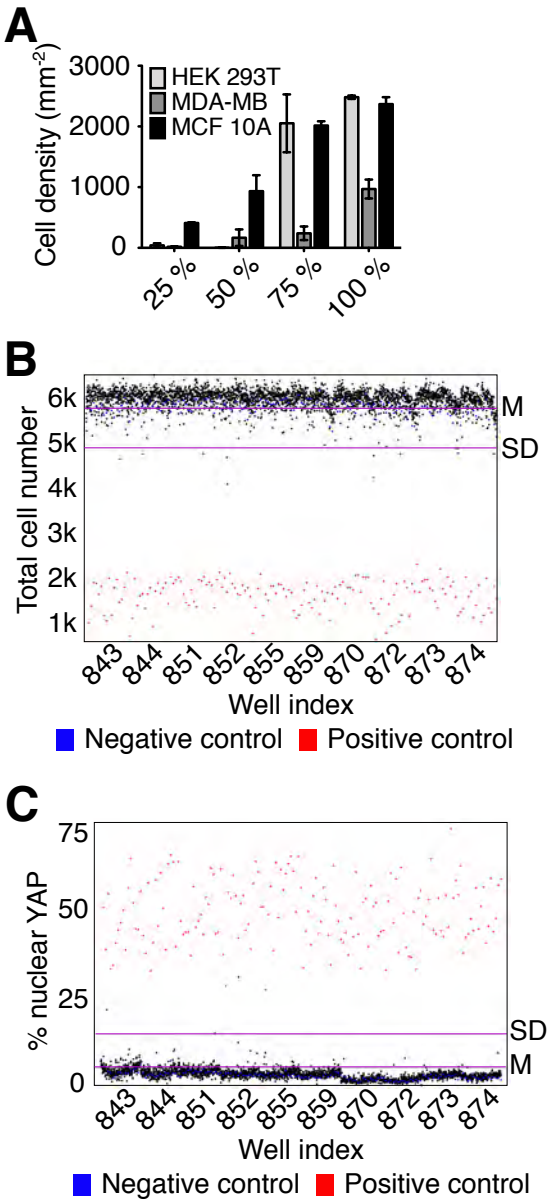

Figure S1. Screening for activators of Yap translocation into nuclei. Related to Figure 1. (A) The adherent properties of three human epithelial-cell lines—one embryonic kidney line (HEK 293T) and two mammary-gland lines (MDA-MB and MCF 10A)—were tested. Only MCF 10A cells display a reproducible correlation between the number of cells seeded and the number of cells adhered after 24 hr. (B) In a representative example of cell survival in ten 384-well plates screened in the assay for nuclear translocation of Yap, the plate indexes are indicated on the *x*-axis and the total number of cells detected in each well of each plate is indicated on the *y*-axis. Purple lines demonstrate the average mean (M) and one standard deviation (SD) below the mean of the number of cells detected in each negative control well (blue dots) of each of the ten plates screened. Red dots represent sub-confluent positive control wells; black dots represent each well treated with a compound. The substances that decreased the number of cells over one SD were eliminated owing to toxicity. (C) In the same ten 384-well plates analyzed in panel B, the percentage of cells with nuclear Yap was determined using MetaXpress software. Only one in a thousand compounds increased this value more than one standard deviation (SD; purple line) above the mean value determined for the negative controls (M; purple line).

bioRxiv preprint doi: https://doi.org/10.1101/2020.02.11.944157; this version posted February 12, 2020. The copyright holder for this preprint (which was not certified by peer review) is the author/funder, who has granted bioRxiv a license to display the preprint in perpetuity. It is made available under aCC-BY-NC-ND 4.0 International license.

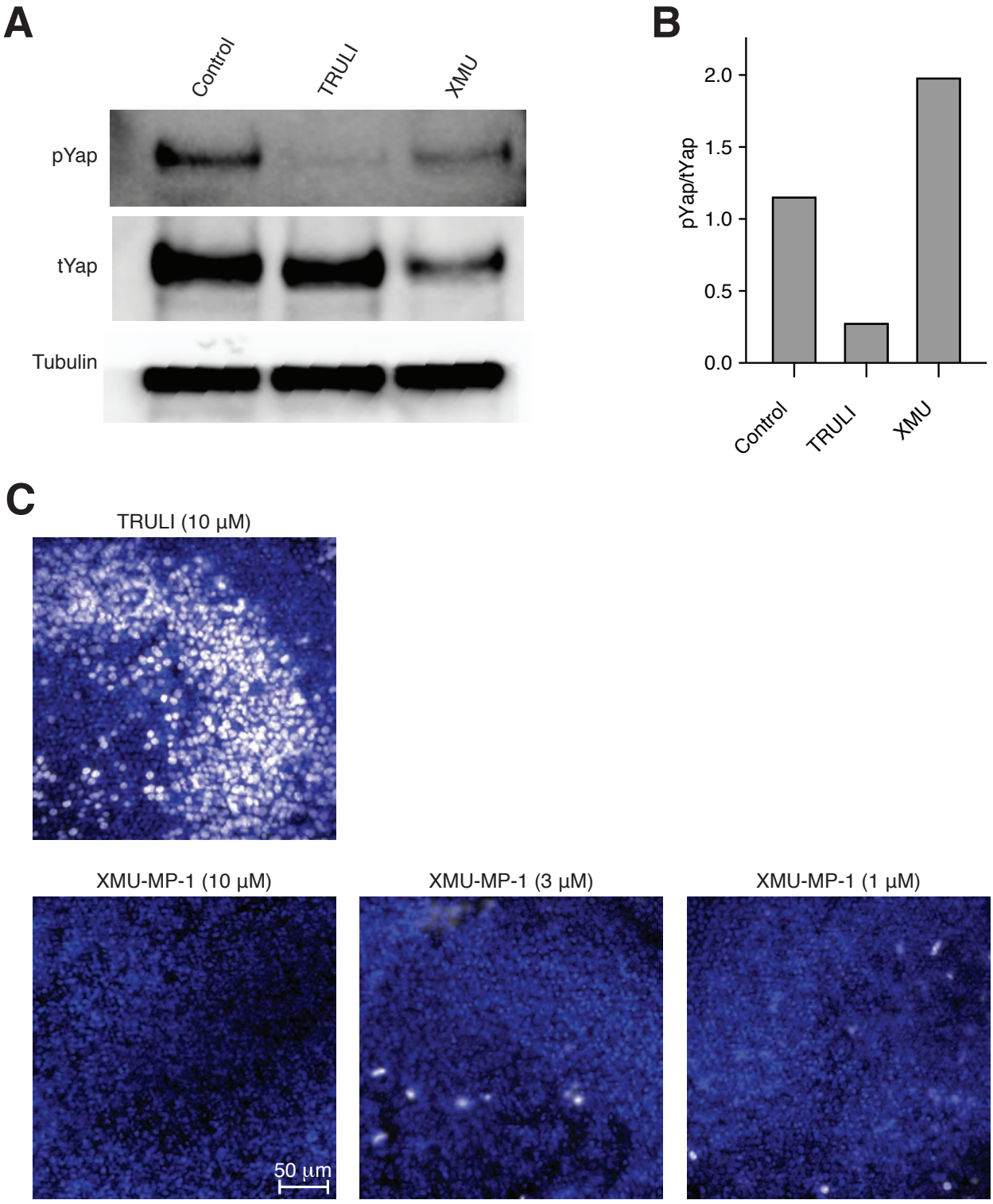

Figure S2. Lack of Yap activation by the Mst inhibitor XMU-MP-1. Related to Figure 2. (A) Six utricles per condition were treated for 24 hr with 10 μM TRULI or XMU-MP-1 to assess effects on the amount of phospho-Yap by comparison to control conditions. (B) Quantification of band-intensity ratios for phospho-Yap and total Yap in the immunoblot of panel A shows that XMU-MP-1 does not reduce the fraction of phosphorylated Yap. (C) When adult mouse utricles were explanted and cultured with EdU (white) and either TRULI or varying concentrations of XMU-MP-1, the latter caused no increase in proliferation. Nuclei are stained with DAPI (blue).

bioRxiv preprint doi: https://doi.org/10.1101/2020.02.11.944157; this version posted February 12, 2020. The copyright holder for this preprint (which was not certified by peer review) is the author/funder, who has granted bioRxiv a license to display the preprint in perpetuity. It is made available under aCC-BY-NC-ND 4.0 International license.

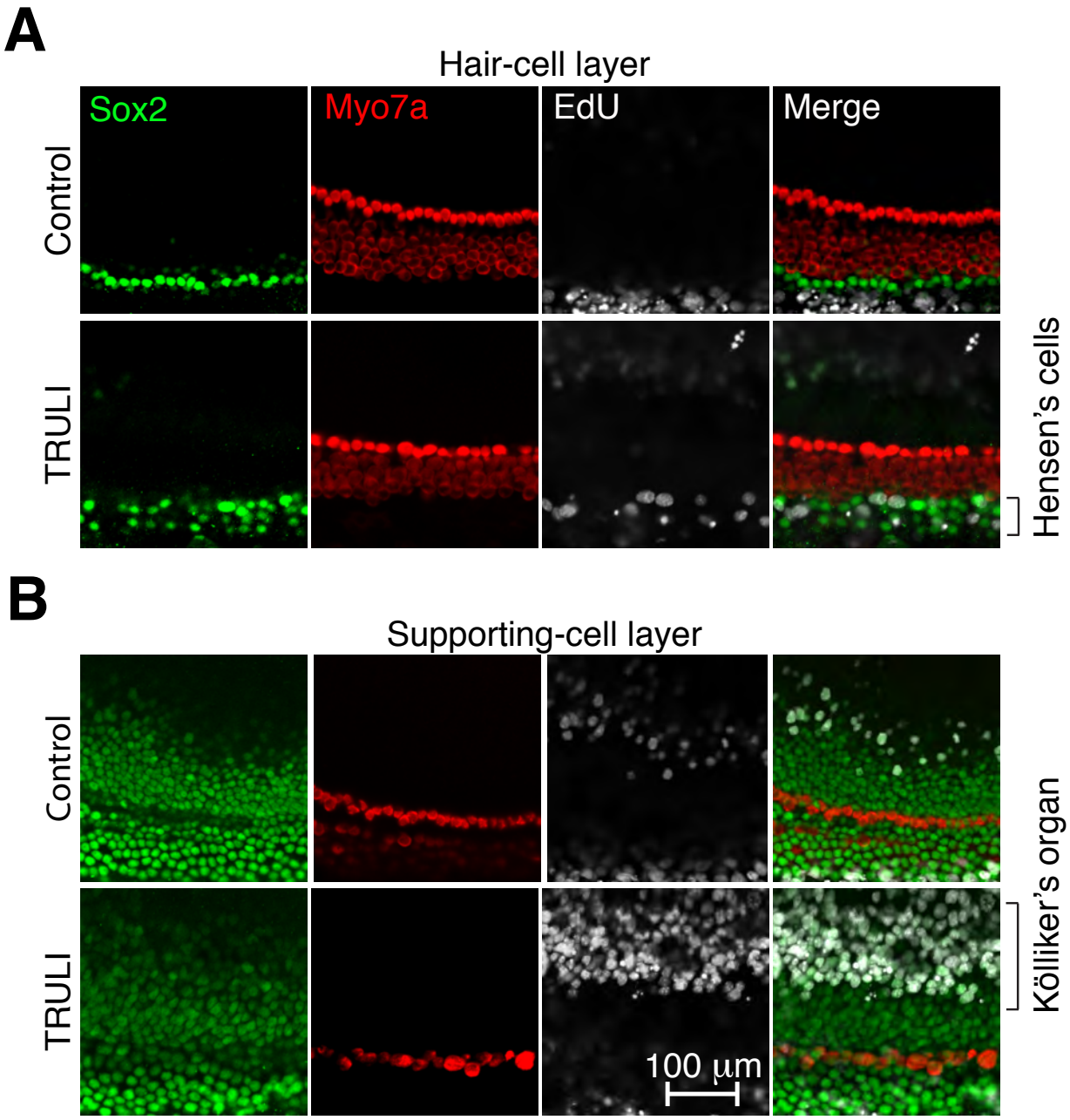

Figure S3. Proliferative response in the cochlea after treatment with TRULI. Related to Figure 2. (A) No hair-cell loss is observed after 5 d of treatment of the P1 organ with 10 μM TRULI. Only the most lateral rows of Hensen's cells re-enter the cell cycle after the treatment. (B) TRULI elicits robust proliferation of Sox2-positive cells in Kölliker's organ, as measured by the incorporation of EdU.

bioRxiv preprint doi: https://doi.org/10.1101/2020.02.11.944157; this version posted February 12, 2020. The copyright holder for this preprint (which was not certified by peer review) is the author/funder, who has granted bioRxiv a license to display the preprint in perpetuity. It is made available under aCC-BY-NC-ND 4.0 International license.

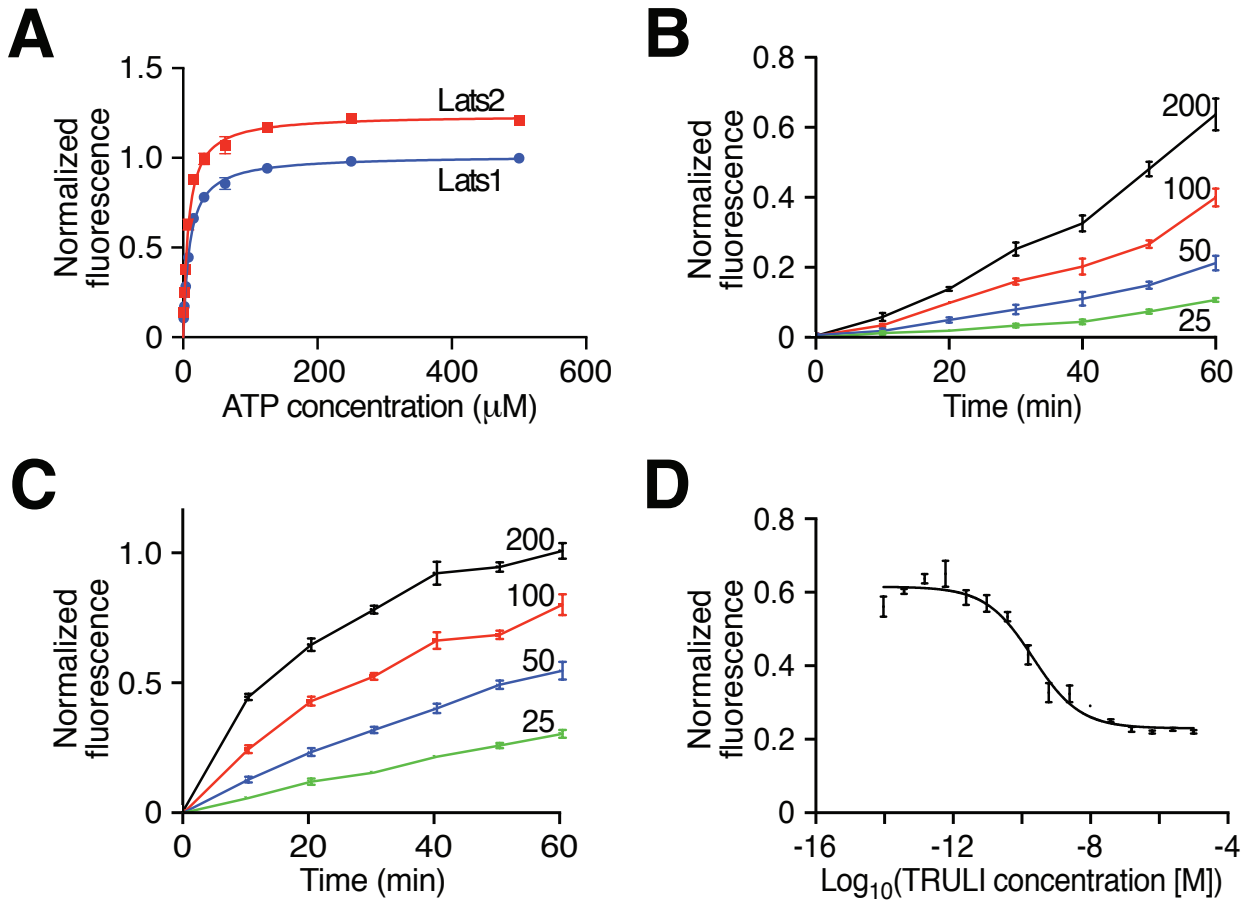

Figure S4. Optimization and further results of *in vitro* kinase assay. Related to Figure 3. (A) In order to perform assays at an appropriate ATP concentration, we established the Michaelis-Menten constants for Lats1 (K_m = 9.4 μM) and Lats2 (K_m = 7.6 μM). (B) A kinetic assay for Lats1 was used to determine the optimal signal-to-noise ratio within the linear range of product formation. Enzyme concentrations are indicated in micrograms per liter. (C) The corresponding assay was performed for Lats2. (D) The half-maximal inhibitory concentration of TRULI against Lats2 was IC_{50} = 0.2 nM.

bioRxiv preprint doi: https://doi.org/10.1101/2020.02.11.944157; this version posted February 12, 2020. The copyright holder for this preprint (which was not certified by peer review) is the author/funder, who has granted bioRxiv a license to display the preprint in perpetuity. It is made available under aCC-BY-NC-ND 4.0 International license.

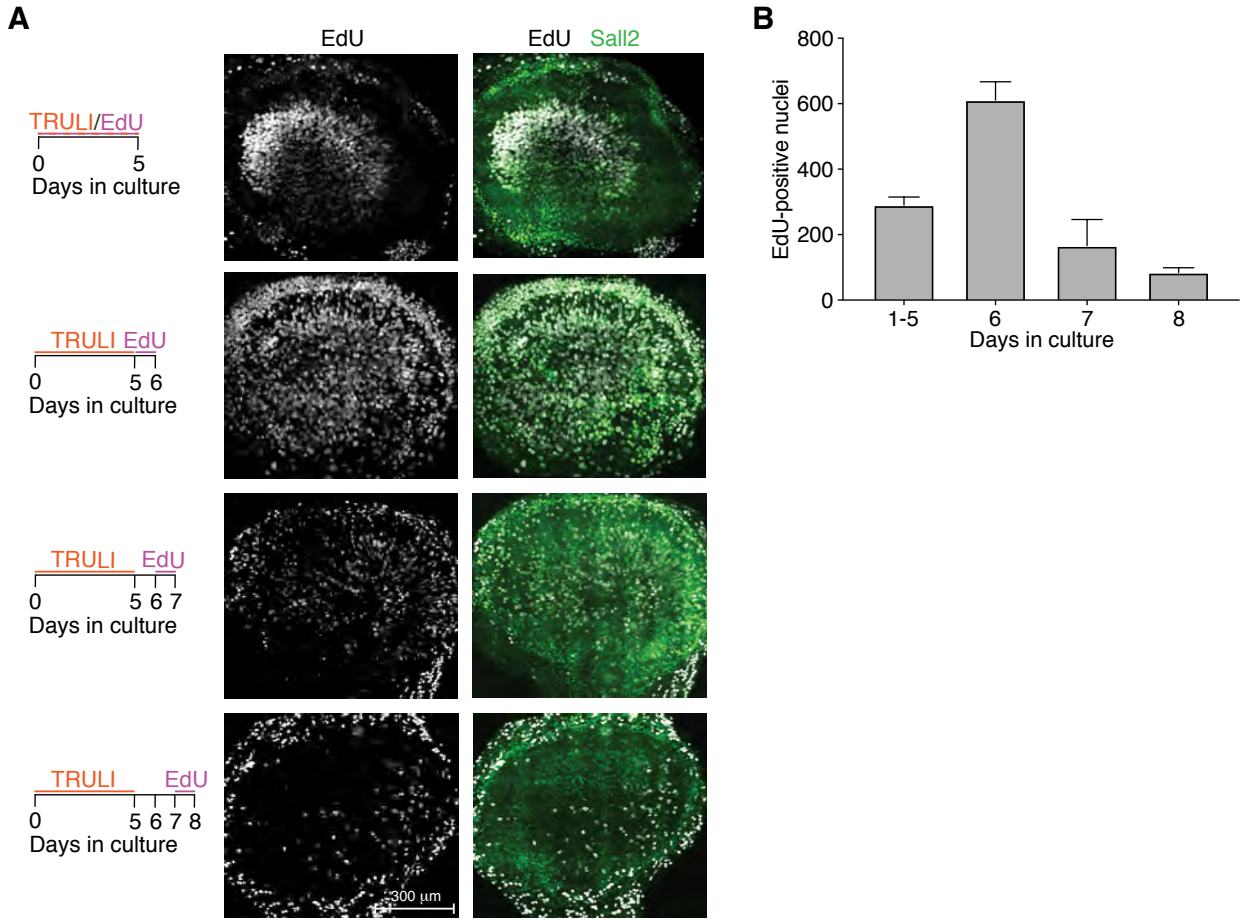

Figure S5. Cell-cycle exit after TRULI withdrawal. Related to Figure 4. (A) As shown in the timelines to the left, utricles were explanted and cultured for 5 d in the presence of TRULI; EdU was then added at various times. In first top row, when EdU was present throughout the 5 d period of culture, extensive proliferation occurred in the striolar region. The second row shows that proliferation was still heavier when EdU was presented during the day following TRULI exposure. The third row indicates that proliferation declined during the second day after TRULI withdrawal. The fourth row demonstrates that proliferation fell to nearly the background level when EdU was provided three days after the withdrawal of TRULI. (B) A bar graph quantifies the number of EdU-positive nuclei per sensory epithelium in the foregoing experiments. Each datum is an average from two utricles.

bioRxiv preprint doi: https://doi.org/10.1101/2020.02.11.944157; this version posted February 12, 2020. The copyright holder for this preprint (which was not certified by peer review) is the author/funder, who has granted bioRxiv a license to display the preprint in perpetuity. It is made available under aCC-BY-NC-ND 4.0 International license.

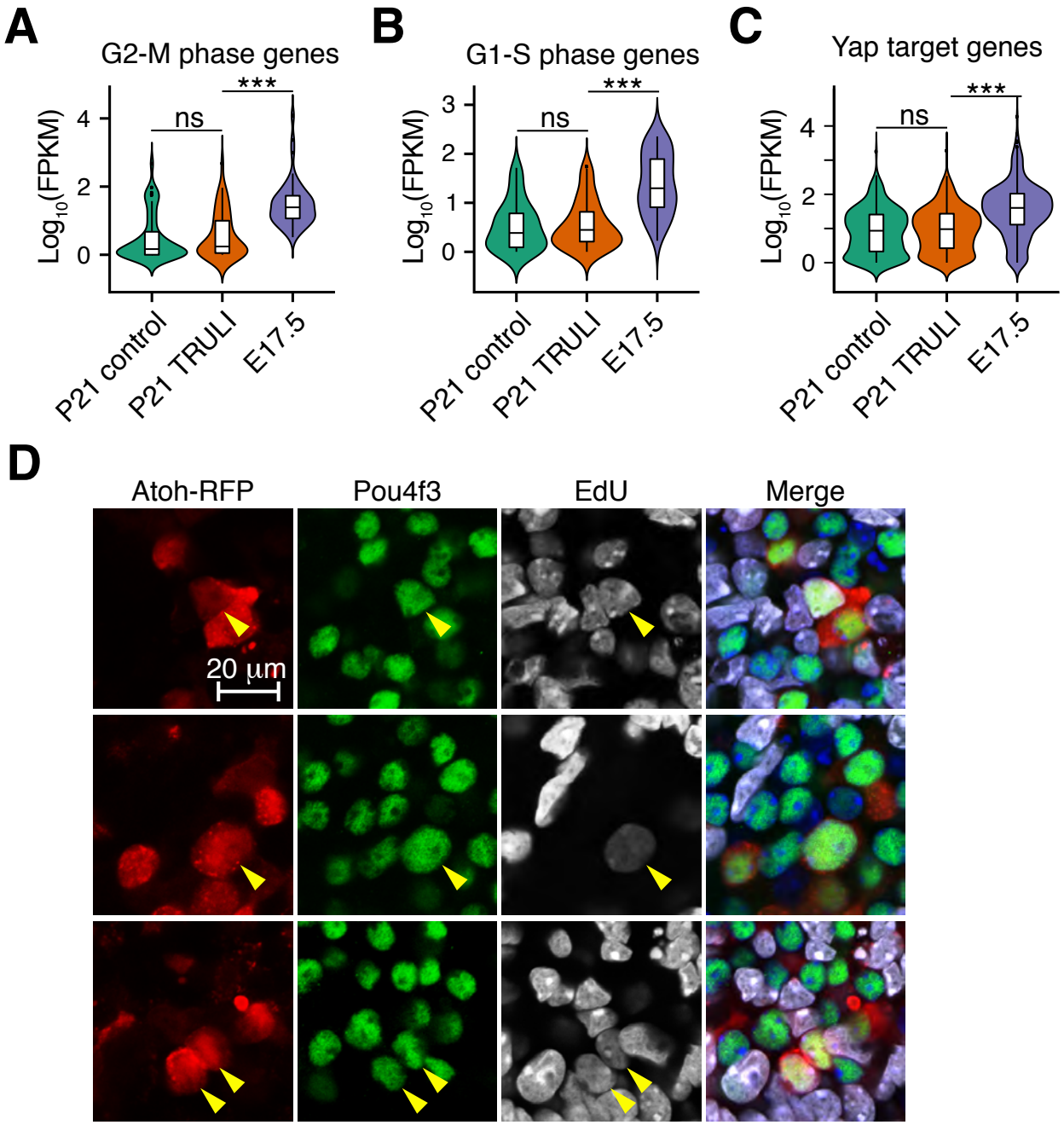

Figure S6. Cell-cycle exit and hair cell differentiation after TRULI withdrawal. Related to Figure 5. (A) RNA-sequencing analysis demonstrates that the genes active in G2-M are downregulated to the control levels in P21 supporting cells 5 d after TRULI withdrawal. (B) S-phase genes are similarly downregulated. (C) Genes known to be targets of theYap-Tead complex are also downregulated. (D) To assess whether new hair cells can be formed after TRULI treatment, P21 utricles that had been treated with TRULI for 5 d were cultured for two days to allow cell-cycle exit, then transfected with adenovirus carrying Atoh1. The cultures were co-treated with EdU to permit lineage tracing of supporting cells that had undergone cell division in the presence of TRULI. After 5 d of Atoh1 expression, many EdU-positive supporting cells displayed high levels of Pou4f3 protein, demonstrating the potential of supporting cells to transdifferentiate.

bioRxiv preprint doi: https://doi.org/10.1101/2020.02.11.944157; this version posted February 12, 2020. The copyright holder for this preprint (which was not certified by peer review) is the author/funder, who has granted bioRxiv a license to display the preprint in perpetuity. It is made available under aCC-BY-NC-ND 4.0 International license.

Table S1. Alignment of residues at the ATP-binding sites of AGC kinases. Related to Figure 3. These 36 residues define the ATP-binding pockets of 62 kinases, but do not represent continuous sequences.

LATS1	LGIGAFGEVAKVRLFVMDYIPGGDMMSDKDNLTDFG
LATS2	LGIGAFGEVAKVKLFVMDYIPGGDMMSDKDNLTDFG
NDR1	IGRGAFGEVAKVKMLIMEFLPGGDMMTDKDNLSDFG
NDR2	IGRGAFGEVAKVKMLIMEFLPGGDMMTDKDNLSDFG
ROCK1	IGRGAFGEVAKVQLMVMEYMPGGDLVNDKDNLADFG
ROCK2	IGRGAFGEVAKVQLMVMEYMPGGDLVNDKDNLADFG
RSKL2	VQDPATGGTMKSSGPHLNLLTPARLPSDHGNLTYFG
SgK494	VAKGSFGTVAKHSLIMCSYCSTDLYSLDKENLTDFG
PDK1	LGEGSFSTVAKVKLFGLSYAKNGELLKDKENLTDFG
RSK4	LGQGSFGKVAKVKLLILDFLRGGDVFTDKENLTDFG
RSK1	LGQGSYGKVAKVKLLILDFLRGGDLFTDKENLTDFG
RSK3	LGQGSFGKVAKVKLLILDFLRGGDLFTDKENLTDFG
RSK2	LGQGSFGKVAKVKLLILDFLRGGDLFTDKENLTDFG
p70S6K	LGKGGYGKVAKVDLLILEYLSGGELFMDKENMTDFG
p70S6Kb	LGKGGYGKVAKVELLILECLSGGELFTDKENMTDFG
MSK1	LGTGAYGKVAKVTLLILDYINGGELFTDKENLTDFG
MSK2	LGTGAYGKVAKVTLLILDYVSGGEMFTDKENLTDFG
YANK2	IGKGSFGKVAKVNLMVVDLLLGGDLRYDKDNLTDFN
YANK3	IGKGSFGKVAKVNLMVVDLLLGGDLRYDKDNLTDFN
YANK1	IGKGSFGKVAKVNLMVVDLLLGGDLRYDKDNLTDFN
PKCi	IGRGSYAKVAKVGLFVIEYVNGGDLMFDKDNLTDYG
PKCz	IGRGSYAKVAKVGLLVIEYVNGGDLMFDKDNLTDYG
SGK2	IGKGNYGKVAKVGLFVLDYVNGGELFFDKENLTDFG
SGK	IGKGSFGKVAKVGLFVLDYINGGELFYDKENLTDFG
SGK3	IGKGSFGKVAKVGLFVLDFVNGGELFFDKENLTDFG
PKN3	LGRGHFGKVAKLSLFVTEFVPGGDLMMDKDNLADFG
PKN2	LGRGHFGKVAKVNLFVMEYAAGGDLMMDKDNLADFG
PKN1	LGRGHFGKVAKVNLFVMEYSAGGDLMLDKDNLADFG
AKT1	LGKGTFGKVAKTALFVMEYANGGELFFDKENMTDFG
AKT2	LGKGTFGKVAKTALFVMEYANGGELFFDKENMTDFG
AKT3	LGKGTFGKVAKTSLFVMEYVNGGELFFDKENMTDFG
PKCt	LGKGSFGKVAKTHMFVMEYLNGGDLMYDKDNLADFG
PKCd	LGKGSFGKVAKTHLFVMEFLNGGDLMYDKDNLADFG
PKCe	LGKGSFGKVAKTQLFVMEYVNGGDLMFDKDNLADFG
PKCh	LGKGSFGKVAKTQLFVMEFVNGGDLMFDKDNLADFG
PKCg	LGKGSFGKVAKTQLFVMEYVTGGDLMYDKDNMTDFG
PKCb	LGKGSFGKVAKTQLFVMEYVNGGDLMYDKDNMADFG
PKCa	LGKGSFGKVAKTQLFVMEYVNGGDLMYDKDNMADFG
BARK2	IGRGGFGEVAKVCMFILDLMNGGDLHYDKANLSDLG
BARK1	IGRGGFGEVAKVCMFILDLMNGGDLHYDKANLSDLG
RHOK	LGKGGFGEVAKVSLLVMTIMNGGDIRYDKENLSDLG
GPRK7	LGKGGFGEVAKVSLLVMSLMNGGDLKFDKENLSDLG
GPRK6	LGKGGFGEVAKVSLLVLTLMNGGDLKFDKENLSDLG
GPRK5	LGKGGFGEVAKVNLLVLTIMNGGDLKFDKENLSDLG
GPRK4	LGKGGFGEVAKVSLLVLTIMNGGDLKFDKENLSDLG
MAST3	ISNGAYGAVAKVSMMVMEYVEGGDCATDKDNLTDFG
MAST4	ISNGAYGAVAKVSMMVMEYVEGGDCATDKDNLTDFG
MAST2	ISNGAYGAVAKVSMMVMEYVEGGDCATDKDNLTDFG
MAST1	ISNGAYGAVAKVGMMVMEYVEGGDCATDKDNLTDFG
CRIK	VGCGHFAEVAKPQLLVMEYQPGGDLLSDKENLVDFG
MASTL	ISRGAFGKVAKVHLLVMEYLIGGDVKSDKDNLTDFG
DMPK1	IGRGAFSEVAKTQLLVMEYYVGGDLLTDKDNLADFG
MRCKb	IGRGAFGEVAKTALLVMDYYVGGDLLTDKDNLADFG
DMPK2	IGRGAFGEVAKTTLLVMDYYAGGDLLTDKDNLADFG
MRCKa	IGRGAFGEVAKTTLLVMDYYVGGDLLTDKDNLADFG
PKG2	LGVGGFGRVAKVKLMLLEACLGGELWSDKENIVDFG
PKG1	LGVGGFGRVAKVRLMLMEACLGGELWTDKENIVDFG
PRKX	VGTGTFGRVAKIRLMLMEYVPGGELFSDKENLTDFG
PRKY	MGTGTFGRVAKIRLMLMEYVPGGELFSDKENLTDFG
PKACg	LGMGSFGRVAKVKLLVMEYVPGGEMFSDKENLTDFG
PKACb	LGTGSFGRVAKVRLMVMEYVPGGEMFSDKENLTDFG
PKACa	LGTGSFGRVAKVKLMVMEYVPGGEMFSDKENLTDFG

bioRxiv preprint doi: https://doi.org/10.1101/2020.02.11.944157; this version posted February 12, 2020. The copyright holder for this preprint (which was not certified by peer review) is the author/funder, who has granted bioRxiv a license to display the preprint in perpetuity. It is made available under aCC-BY-NC-ND 4.0 International license.

Table S2. Percentage sequence identity for the 36 residues of the ATP-binding site between Lats1 and Lats2 and AGC kinases. Related to Figure 3. In this and the subsequent two tables, colors identify different sub-families of the AGC kinase family.

AGC kinase	Identity to Lats1 (%)	Identity to Lats2 (%)
LATS1	100.0	97.2
LATS2	97.2	100.0
PKACb	75.0	72.2
PKN2	72.2	72.2
PKN1	72.2	72.2
ROCK1	72.2	72.2
ROCK2	72.2	72.2
PKACg	72.2	75.0
PKACa	72.2	75.0
PKCe	69.4	69.4
PKCg	69.4	69.4
NDR1	69.4	72.2
NDR2	69.4	72.2
MASTL	69.4	69.4
MRCKb	69.4	69.4
DMPK2	69.4	69.4
MRCKa	69.4	69.4
SGK	66.7	66.7
PKN3	66.7	66.7
PKCt	66.7	66.7
PKCd	66.7	66.7
PKCh	66.7	66.7
PKCb	66.7	66.7
PKCa	66.7	66.7
MSK1	63.9	63.9
MSK2	63.9	63.9
CRIK	63.9	63.9
DMPK1	63.9	63.9
PRKX	63.9	61.1
PRKY	63.9	61.1
RSK4	61.1	63.9
RSK3	61.1	63.9
RSK2	61.1	63.9
YANK2	61.1	61.1
YANK3	61.1	61.1
YANK1	61.1	61.1
PKCi	61.1	61.1
SGK2	61.1	61.1
SGK3	61.1	61.1
AKT1	61.1	61.1
AKT2	61.1	61.1
AKT3	61.1	61.1
RHOK	61.1	61.1
GPRK7	61.1	61.1
MAST3	61.1	61.1
MAST4	61.1	61.1
MAST2	61.1	61.1
MAST1	61.1	61.1
RSK1	58.3	61.1
PKCz	58.3	58.3
GPRK6	58.3	58.3
GPRK5	58.3	58.3
GPRK4	58.3	58.3
PDK1	55.6	58.3
BARK2	55.6	55.6
BARK1	55.6	55.6
PKG1	55.6	52.8
p70S6K	52.8	52.8
PKG2	52.8	55.6
p70S6Kb	50.0	50.0
SgK494	44.4	44.4
RSKL2	27.8	27.8

bioRxiv preprint doi: https://doi.org/10.1101/2020.02.11.944157; this version posted February 12, 2020. The copyright holder for this preprint (which was not certified by peer review) is the author/funder, who has granted bioRxiv a license to display the preprint in perpetuity. It is made available under aCC-BY-NC-ND 4.0 International license.

Table S3. Target enzymes binding more potently than LATS1. Related to Figure 3. Of 314 kinases in a binding panel, these enzymes bound 1 μM TRULI more strongly than did Lats1 or Lats2. The assay did not test for functional inhibition.

Kinase	Affinity
CLK4	102.191
PRKCQ	99.155
CDC7	99.093
DMPK	97.919
CDC42BPA	97.161
HIPK3	95.798
HIPK2	94.205
PRKACB	92.922
CLK2	92.819
GSK3B	92.698
PRKCH	90.416
CDK19	90.205
PKN2	89.660
CDK8	88.778
PRKX	88.131
BMP2K	86.274
HIPK1	86.064
DYRK1A	85.826
PASK	85.771
ROCK2	84.111
CDC42BPG	83.657
PAK4	83.440
DYRK1B	81.514
TGFBR2	81.311
LRRK2	81.277
ROCK1	79.232
PRKG2	79.109
CLK1	78.062
PRKCD	77.995
PKN1	77.735
MAP4K4	77.535
DAPK3	77.096
TAOK1	76.404
LATS2	74.882
MAP3K7	74.047
LATS1	73.903

bioRxiv preprint doi: https://doi.org/10.1101/2020.02.11.944157; this version posted February 12, 2020. The copyright holder for this preprint (which was not certified by peer review) is the author/funder, who has granted bioRxiv a license to display the preprint in perpetuity. It is made available under aCC-BY-NC-ND 4.0 International license.

Table S4. Half-maximal inhibitory concentrations (*IC*$_{50}$s) of TRULI for selected kinases. Related to Figure 3.

Kinase	*IC*$_{50}$ (nM)
PKA	60
PKCepsilon	14
ROCK1	88
NDR1	1000